Development of an inhibitory TTC7B selective nanobody that blocks EFR3 recruitment of PI4KA

Sushant Suresh[1], Alexandria L Shaw[1,2], Damilola K Akintola[1], Martine Lunke[1], Calvin K Yip[2], Jennifer A Cobb[1], John E Burke[1,2,3]

[1] Department of Biochemistry and Microbiology, University of Victoria, Victoria, BC, V8W 2Y2, Canada

[2] Department of Biochemistry and Molecular Biology, The University of British Columbia, Vancouver, BC, V6T 1Z3, Canada

[3]University of Victoria Genome BC Proteomics Centre, Victoria, BC, Canada

John E Burke jeburke@uvic.ca: Lead contact: John E Burke jeburke@uvic.ca

Abstract

Phosphatidylinositol 4 kinase IIIα (PI4KIIIα/PI4KA) is an essential lipid kinase that plays a critical role in regulating plasma membrane identity. PI4KA is primarily recruited to the plasma membrane through the targeted recruitment by the proteins, EFR3A and EFR3B, which bind to the PI4KA accessory proteins TTC7 (TTC7A/B) and FAM126 (FAM126A/B). Here we characterised how both EFR3 isoforms interact with all possible TTC7-FAM126 combinations and developed a nanobody that specifically blocked EFR3-mediated PI4KA recruitment in TTC7B containing complexes. Most EFR3-TTC7-FAM126 combinations show similar binding affinities, with the exception of EFR3A-TTC7B-FAM126A, which binds with a ~10-fold higher affinity. Moreover, we showed that EFR3B phosphorylation markedly decreased binding to TTC7-FAM126. Using a yeast display approach, we isolated a TTC7B selective nanobody that blocked EFR3 binding. Cryo-electron microscopy and hydrogen deuterium exchange mass spectrometry revealed that this nanobody sterically blocked EFR3 recruitment and showed an extended interface with both PI4KA and TTC7B. Collectively, these findings provide new insights into PI4KA regulation and provide a tool for manipulating PI4KA complexes, that may be valuable for therapeutic targeting.

Running title:

Allosteric targeting of the EFR3 binding site of the PI4KA complex

Keywords:

PI4KA, TTC7A, TTC7B, FAM126A, HDX-MS, Cryo-EM, PI4P, nanobody

Introduction

Phosphoinositides are critical mediators of many biological processes at the plasma membrane (PM), with the lipid phosphatidylinositol 4-phosphate (PI4P) being an essential PM lipid, and it is generated by the lipid kinase type III phosphatidylinositol 4 kinase (referred to by its gene name PI4KA) (1–3). PI4P is essential for defining the lipid identity of the PM (4), and it is the precursor for the downstream signaling lipids, PIP_2 and PIP_3, which play crucial roles in multiple signaling processes (5). The generation of PI4P at the PM is essential for enrichment of phosphatidylserine (PS) as PI4P provides the energy necessary for transport of PS from the ER against its concentration gradient (6). The predominant form of PI4KA exists as a complex with its accessory proteins, TTC7 (two possible isoforms TTC7A and TTC7B) and FAM126 (two possible isoforms FAM126A and FAM126B). The PI4KA complex is a ~750 kDa dimer of heterotrimers, referred to here as the PI4KA complex (7, 8). Both TTC7 and FAM126 contribute towards complex stability, with FAM126 not directly interacting with PI4KA, but instead acting as a stabilizer of TTC7 (9). The PI4KA complex has to be recruited to the PM for its activity (10), primarily through interactions with palmitoylated EFR3 proteins (two isoforms EFR3A and EFR3B). This recruitment of the PI4KA complex to the plasma membrane is mediated by the C-terminus of EFR3 interacting with both TTC7 and FAM126 (11).

Misregulation of PI4KA and its regulatory partners have been heavily implicated in multiple human diseases (12, 13), with diseases driven by both loss-of-function and gain-of-function alterations. These alterations are often isoform and tissue specific. Loss-of-function mutations in TTC7A are found in patients with immunodeficiencies, intestinal

59 artesias and early onset inflammatory bowel disease (IBD) (14–17), and result in a
60 marked reduction in PI4KA activity. However, there are no known mutations in TTC7B
61 linked to disease. Similarly, disease linked mutations are only found in FAM126A and not
62 in FAM126B. Loss-of-function mutations in FAM126A cause hypomyelination and
63 congenital cataract (HCC), a disorder characterized by neurological impairment, cognitive
64 defects and peripheral neuropathy (18–20). Conversely, overactivation of PI4KA
65 signaling is also involved in disease. In Hepatitis C viral infection, the viral protein NS5A
66 activates PI4KA, leading to the formation of viral replication organelles enriched in PI4P
67 (21, 22). Increased PI4KA activity also plays a role in cancer, with overexpression of
68 PI4KA and EFR3A implicated in KRAS driven pancreatic cancers (23, 24). Interestingly,
69 EFR3A interacts with oncogenic KRAS promoting tumorigenic activity (23), with this
70 proposed to be mediated by increased PS levels at the PM (24). The role of PI4KA and
71 EFR3A in driving KRAS driven cancers has renewed enthusiasm in generating
72 pharmacological agents that turn off PI4KA signaling in combination with KRAS mutant
73 selective inhibitors.

74 PI4KA inhibitors were originally developed as anti-Hepatitis C viral inhibitors,
75 leading to development of multiple wall validated potent and selective PI4KA inhibitors
76 (25, 26). However, enthusiasm for these molecules as therapeutics was greatly
77 diminished as knockdown of PI4KA either genetically or pharmacologically caused rapid
78 death in mice driven by severe gastrointestinal side effects and dramatically decreased
79 PM PIP_2 levels (26). While there may be possibilities to target PI4KA signaling in EFR3A
80 driven tumors, the severe side effects of ATP competitive PI4KA inhibitors suggests there
81 could be advantages of novel allosteric PI4KA modulators. The development of molecules
82 that block EFR recruitment of PI4KA offers a potential avenue to design novel
83 therapeutics, and provides opportunities to further understand how PI4KA is regulated.
84 One of the most well validated tools to manipulate signaling proteins are nanobodies,
85 which bind to specific effector interfaces, leading to modulators of intracellular signaling
86 pathways. Nanobodies are composed of the variable domains (VHH) of heavy chain only
87 antibodies (HCAbs) that lack the light chain of conventional antibodies (27). The single
88 domain architecture results in a compact size (~15 kDa) that can be readily expressed in

89 bacteria with high yield, making them an attractive tool for therapeutic and diagnostic
90 applications (28).

91 Understanding regulation of the PI4KA complex requires insight into how different
92 isoforms of its accessory proteins influence plasma membrane recruitment, along with
93 the development of tools to selectively target these isoforms. Here, we have
94 systematically characterized all possible combinations of PI4KA accessory protein
95 isoforms and determined the EFR3A-TTC7B-FAM126A complex as the highest affinity
96 complex. Using a yeast surface display approach, we purified a TTC7B selective
97 nanobody that blocked EFR3 binding. Using a synergy of cryo-electron microscopy (cryo-
98 EM) and hydrogen-deuterium exchange mass spectrometry (HDX-MS), we identified the
99 binding epitopes of this nanobody on PI4KA, TTC7B and FAM126A and the
100 conformational dynamics upon nanobody binding. Overall, this study provides proof-of-
101 concept that PI4KA activity can be modulated with molecules outside the ATP binding
102 site and introduces a useful isoform-specific nanobody tool to dissect the functional roles
103 of PI4KA accessory proteins in controlling PI4KA activity.

104

105 **Results**

106 ***EFR3A binds with highest affinity towards TTC7B-FAM126A***

107 The structure of EFR3A bound to the complex of PI4KA with TTC7B and FAM126A
108 suggested that there may be differential affinities of unique EFR3 isoforms to different
109 TTC7 and FAM126 isoforms. This was based on the C-terminal interacting region of
110 EFR3 binding to both TTC7 and FAM126 (11), with the interacting regions in EFR3, TTC7
111 and FAM126 being highly conserved, but not strictly conserved between isoforms. The
112 different isoforms of EFR3, TTC7, and FAM126 exhibit tissue-specific expression
113 patterns, suggesting distinct physiological roles. Although there are eight possible unique
114 EFR3-TTC7-FAM126 complexes, it remains unclear whether they differ in association.
115 To investigate potential differences in affinity between isoform complexes, we purified
116 different combinations of TTC7 and FAM126, as well as MBP tagged C-terminal
117 fragments of EFR3A (721-791) and EFR3B (716-787) (**Fig 1A**). The dimers of TTC7B

118 with FAM126A (1-308) or FAM126B (1-308) were purified from *E. coli,* with the dimers of
119 TTC7A with FAM126A/B purified from *Sf9* cells. All four dimers eluted from gel filtration
120 at sizes consistent with a heterodimer.

121 We performed bio-layer interferometry (BLI) experiments to measure binding
122 kinetics with His-tagged MBP-EFR3 immobilized on the biosensor tip and TTC7-FAM126
123 as the analyte. For all measurements we used MBP alone as a non-specific binding
124 control. The full binding parameters (K_d, K_{on} and K_{off}) are shown in Table S1. Most of the
125 isoform combinations generated BLI traces that fit well to a 1:1 binding model (**Fig 1B-**
126 **D**), with the only exception being EFR3B binding to TTC7A with either FAM126 isoform
127 (Fig S1). All heterodimers of TTC7 and FAM126 had dissociation constants indicative of
128 relatively similar affinities (~0.3 nM), with a single exception being EFR3A, which showed
129 almost a 10-fold reduction in binding to TTC7B-FAM126A (~0.04 nM) **(Fig. 1B)**. This
130 increased affinity of EFR3A for TTC7B-FAM126A was primarily driven by a decrease in
131 the k_{off} rate for EFR3A-TTC7B-FAM126A.

132 EFR3 isoforms primarily recruit TTC7 and FAM126 in the biologically relevant
133 complex also containing PI4KA, with each complex containing two possible EFR3 binding
134 sites due to PI4KA dimerization. We purified heterotrimers of PI4KA with either TTC7A-
135 FAM126A or TTC7B-FAM126B and tested their binding to the C-terminal fragment of
136 EFR3A. The binding affinity of EFR3A to the PI4KA-TTC7B-FAM126A (0.04 nM) and
137 PI4KA-TTC7A-FAM126A (340 nM) trimers was similar to that of the dimers, further
138 supporting that TTC7B binds to EFR3A more strongly than TTC7A. **(Fig. 1E)**. Overall,
139 these results show that *in vitro,* the highest affinity interaction between possible EFR3,
140 TTC7, and FAM126 isoforms occurs with the combination of EFR3A and TTC7B-
141 FAM126A.

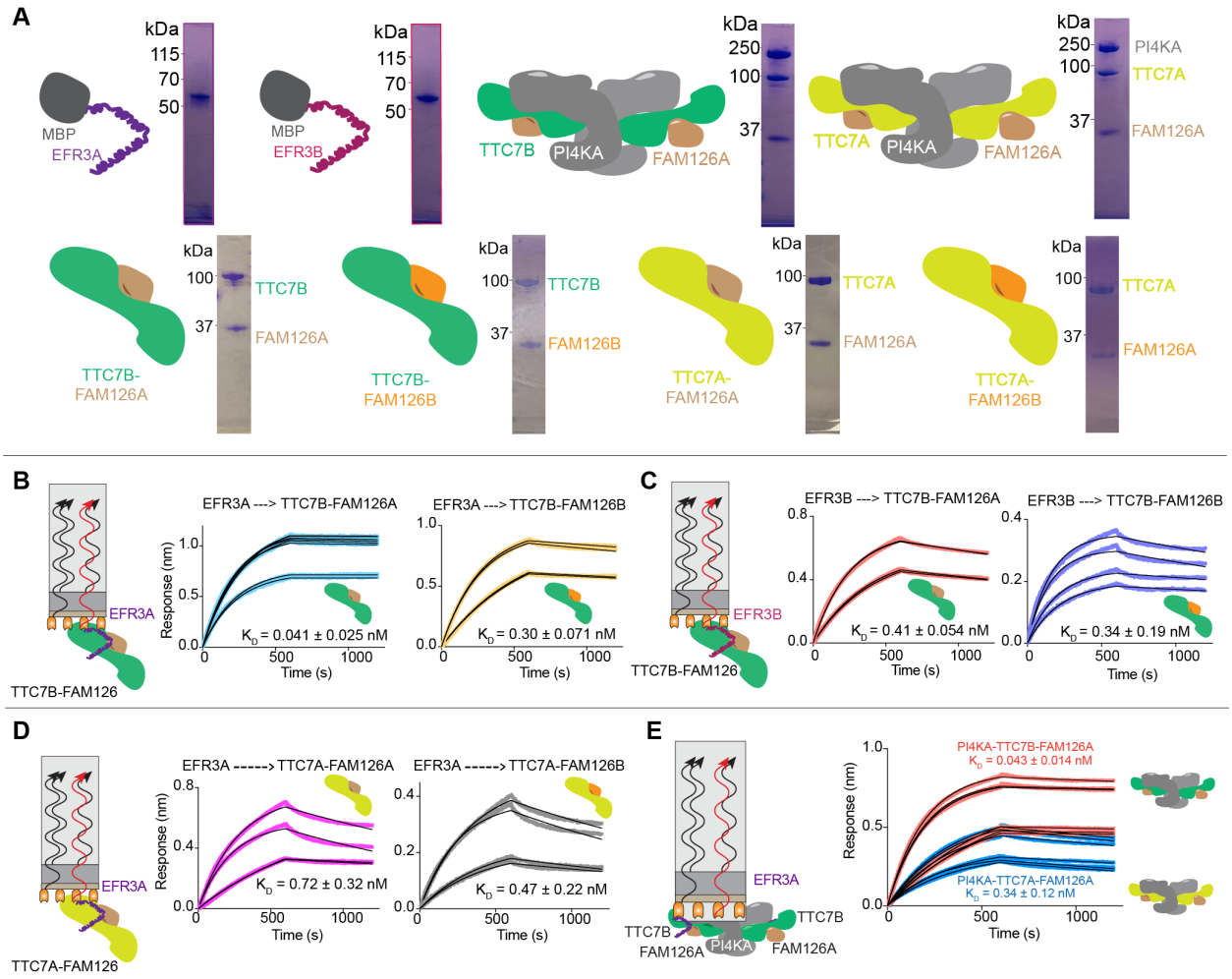

Figure 1. Isoform differences in EFR3

(A) Cartoon representations of the different isoforms of EFR3, TTC7 and FAM126 used in this paper. (L-R) MBP-EFR3A (721-791), MBP-EFR3B (716-787), PI4KA-TTC7B-FAM126A (1-308), PI4KA-TTC7A-FAM126A (1-308), TTC7B-FAM126A (1-308), TTC7B-FAM126B (1-308), TTC7A-FAM126A (1-308), and TTC7B-FAM126B (1-308).

(B) (L) Cartoon of BLI experiment with EFR3A on the tip and TTC7B-FAM126A/B in solution. Raw BLI traces of EFR3A binding to TTC7B-FAM126A/B. The K_D was calculated using a 1:1 binding model.

(C) (L) Cartoon of BLI experiment with EFR3B on the tip and TTC7B-FAM126A/B in solution. Raw BLI traces of EFR3B binding to TTC7B-FAM126A/B. The K_D was calculated using a 1:1 binding model.

154 (D) (L) Cartoon of BLI experiment with EFR3A on the tip and TTC7A-FAM126A/B in solution. Raw
155 BLI traces of EFR3A binding to TTC7A-FAM126A/B. The K_D was calculated using a 1:1 binding
156 model.
157 (E) (L) Cartoon of BLI experiment with EFR3A on the tip and PI4KA complex in solution. (R) Raw
158 BLI traces of EFR3A binding with PI4KA-TTC7A/B-FAM126A (2.5 nM, 5 nM). The K_D was
159 calculated using a 1:1 binding model.
160

161 ***EFR3 recruitment to TTC7-FAM126 can be altered by phosphorylation***

162 Alterations in the affinity of EFR3 isoforms binding TTC7-FAM126 led us to
163 interrogate possible differences between them. We first analyzed the EFR3 C-terminus
164 for potential changes in post-translational modifications that may regulate PI4KA
165 recruitment. In yeast, phosphorylation of Efr3 weakens its interaction with Ypp1 (homolog
166 of TTC7) and inhibits the recruitment of Stt4 (homolog of PI4KA) to the membrane (29).
167 There are several reported EFR3A and EFR3B phosphorylation sites that are located at
168 the interface with TTC7 and FAM126, including Y723 in EFR3B and S738 in EFR3A (30).
169 Y723 in EFR3B lies at the predicted interface with TTC7, where its phosphorylation may
170 disrupt binding due to the proximity of the hydroxyl group to a conserved glutamic acid
171 residue in both TTC7A and TTC7B **(Fig. 2A)**. We used kinase motif analysis to identify
172 possible kinases that may phosphorylate Y723, with it being identified as a likely substrate
173 of multiple Src family kinases (top five scoring kinases: BLK, HCK, FRK, LYN, and LCK)
174 (31). We treated EFR3B with an active construct of the tyrosine kinase LCK, which
175 resulted in predominantly singly phosphorylated species at pY723 (~92%) as determined
176 by MS analysis **(Fig. 2B-C)**. We next performed BLI to measure the binding of phospho-
177 EFR3B to TTC7B-FAM126A and observed a ~90% decrease in binding upon Y723
178 phosphorylation **(Fig. 2D)**. These results demonstrate that phosphorylation of specific
179 EFR3 isoforms may provide another modality to regulate isoform-specific interactions and
180 PI4KA recruitment and activation at the PM.

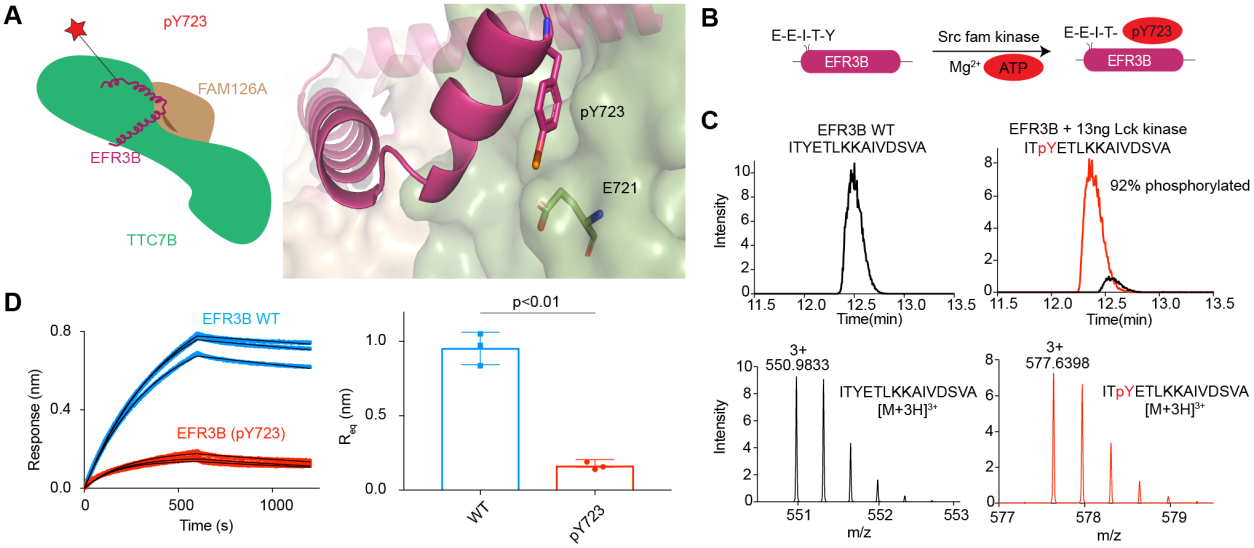

Figure 2. EFR3B phosphorylation decreases TTC7-FAM126 binding

(A) Y723 on EFR3B can be phosphorylated by the Src family kinases. Here, we used LCK, a Src family kinase to phosphorylate Y723 (red) on EFR3B.

(B) (L) Cartoon schematic of EFR3B-TTC7B-FAM126A with Y723 highlighted with a red star. (R) Alphafold3 cartoon of EFR3B-TTC7B-FAM126A showing phosphorylated Y723 on EFR3B and E721 on TTC7B.

(C) Top: Peptide spectra of the unphosphorylated (L) and phosphorylated (R) EFR3B peptide with Y723 highlighted red in the sequence. Bottom: Extracted Ion Chromatograms (EIC) of the EFR3B peptide for unphosphorylated (Black) and phosphorylated (Red).

(D) Raw BLI traces of EFR3B WT (blue) or pY723 (red) binding to TTC7B-FAM126A (L). Maximum BLI response of EFR3B WT and pY723 (R). Error is shown as SD (n = 3) with p value indicated.

Screening of putative inhibitors of PI4KA

Extensive biochemical screening of small molecule libraries resulted in the development of multiple potent, and highly selective, PI4KA inhibitors, although early testing in mouse models revealed severe toxicity (25, 26). More recently, however, it has been proposed that there may be a therapeutic window when these compounds are used in combination with RAS-targeting inhibitors (23, 24). This prompted us to determine whether the two TTC7 isoforms differentially affect complex inhibition in PI4KA-TTC7A/B-FAM126A assemblies. We also tested the FDA approved molecule simeprevir, which has

203 been putatively described as a PI4KA inhibitor (24, 32), although, importantly the
204 published *in vitro* inhibition data did not seem to show profiles consistent with ATP
205 competitive inhibition (32).

206 PI4KA kinase assays were carried out with the three chemical modulators, GSK-
207 A1, GSK-F1, and simeprevir for both PI4KA-TTC7A-FAM126A and PI4KA-TTC7B-
208 FAM126A in the presence of lipid vesicles composed of 100% PI vesicles. Both
209 complexes were inhibited by the GSK-A1 and GSK-F1 compounds, however, we detected
210 no inhibition by simeprevir at concentrations up to 10 μM (**Fig 3**). These results indicate
211 that the two TTC7 isoforms do not differentially affect PI4KA complex inhibition by ATP
212 competitive inhibitors and suggest that previous reports proposing simeprevir as a PI4KA
213 inhibitor should be interpreted with caution.

214

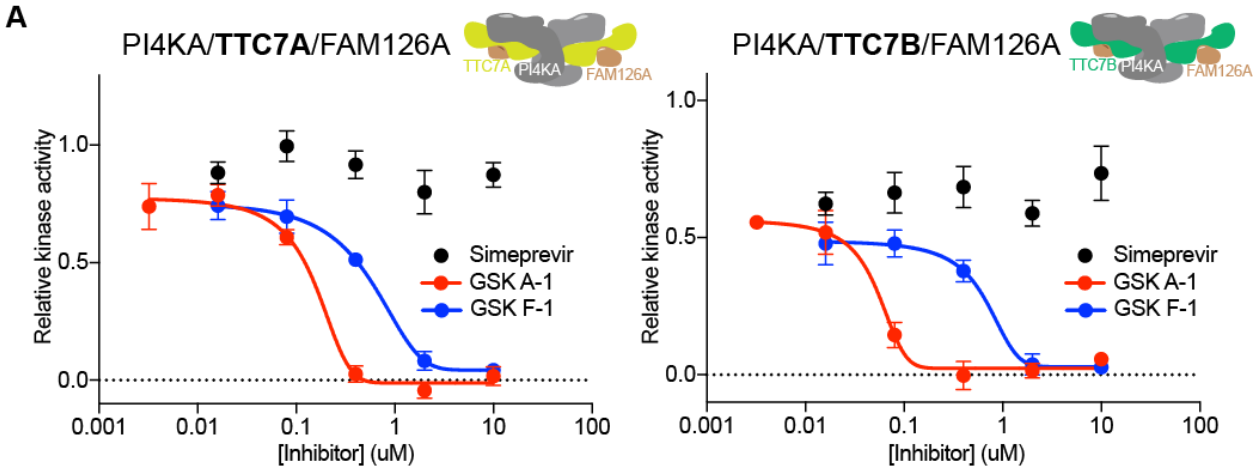

215

216 **Figure 3. Simeprevir does not inhibit PI4KA activity**

217 (A) IC_{50} curves of (L) PI4KA/TTC7A/FAM126A and (R) PI4KA/TTC7B/FAM126A when
218 treated with increasing concentrations of GSK-A1 (red) and GSK-F1 (blue), compared to
219 PI4KA activity when treated with increasing concentrations of simeprevir (black). Assays
220 were carried out with 100% PI vesicles at a final concentration of 0.25 mg/ml in the
221 presence of 100 µM ATP. PI4KA concentration was 5 nM. Error is shown as standard
222 deviation (n=3).

223

224

225 ***Generation of a nanobody that blocks EFR3 recruitment of TTC7B-FAM126A***

226 As the TTC7B-FAM126A isoform showed the highest affinity for EFR3 recruitment,
227 and PI4KA inhibitors showed no differences in inhibition between PI4KA complexes, we
228 sought to develop a tool for selectively targeting unique PI4KA complexes. To address
229 this, we aimed to isolate a nanobody that specifically blocked EFR3 binding to the TTC7B-
230 FAM126A complex. For this purpose, we screened a yeast surface display synthetic
231 library of >5 x 10^8 nanobodies for binders to the EFR3 binding site of TTC7B-FAM126A
232 (33). We used the TTC7B - FAM126A (1-308) heterodimer as our antigen **(Fig. 4A)** and
233 performed multiple rounds of magnetic-activated cell sorting (MACS) and fluorescence-
234 activated cell sorting (FACS) to obtain a library of nanobodies that bound TTC7B-
235 FAM126A **(Fig. 4B)**. To specifically obtain nanobodies that bind at the EFR3 binding site
236 on TTC7B-FAM126A, we purified TTC7B in complex with a chimeric fusion construct
237 comprising FAM126A (1-308) fused to the C-terminus of EFR3A (681-791). The gel
238 filtration elution profile indicated the formation of a heterodimer **(Fig. 4A+C)**. We used this
239 construct to counter-select against our original nanobody library **(Fig. 4B)**, resulting in the
240 isolation of a nanobody that bound TTC7B-FAM126A but not the TTC7B-EFR3A-
241 FAM126A chimera. We named this nanobody, F3IN (E**F**R**3-I**nterfering **N**anobody). BLI
242 confirmed that F3IN binds TTC7B-FAM126A with high affinity, while showing significantly
243 reduced binding to the TTC7B-EFR3A-FAM126A chimera **(Fig. 4D)**.

244 The F3IN nanobody bound to the TTC7B-FAM126A dimer with a K_D of 3.0 ± 0.8
245 nM **(Fig. 4E)**, and showed similar binding to dimers of TTC7B-FAM126B **(Fig. 4F**). In
246 contrast, F3IN showed no detectable binding to TTC7A-FAM126A dimers, indicating
247 isoform selectivity towards TTC7B **(Fig. 4G).** The most physiologically relevant binding
248 interaction of F3IN would be with the PI4KA complex, and we performed BLI experiments
249 with PI4KA trimer in solution. Surprisingly, we found that the F3IN nanobody bound with
250 a ~100-fold increased affinity to the PI4KA-TTC7B-FAM126A complex compared to the
251 TTC7B-FAM126A dimer (K_D of 0.030 ± 0.002 nM to the trimer) **(Fig. 4H)**. In alignment
252 with dimer results, we observed a ~30-fold decrease in affinity of F3IN for PI4KA-TTC7A-
253 FAM126A (0.030 nM for TTC7B versus 1.3 nM for TTC7A complex). Overall, this showed

that the F3IN nanobody is specific for TTC7B over TTC7A and binds with higher affinity to the PI4KA heterotrimer over the TTC7-FAM126 dimer.

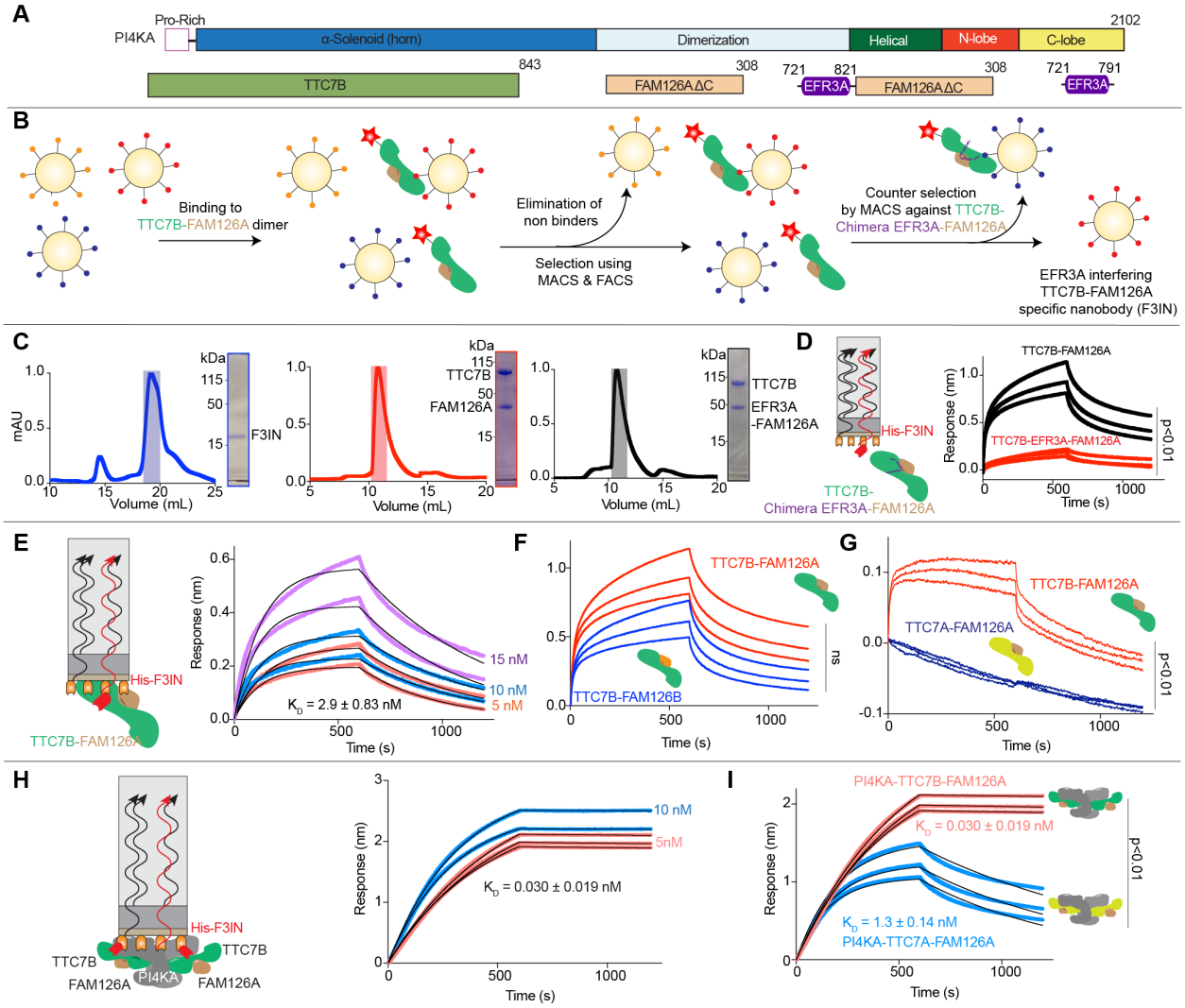

Figure 4. TTC7B selective nanobody generation using yeast surface display

(A) Domain schematics of PI4KA-TTC7B-FAM126A (1-308) (referred to as PI4KA complex), EFR3A (721-791) and Chimeric EFR3A-FAM126A constructs used in this paper.

(B) Schematic of the nanobody selection process using yeast surface display. Antigen is shown with a fluorescent tag (red star). Nanobodies with affinity to antigen are selected using MACS and FACS. Counter selection was performed against chimeric TTC7B-EF3A-FAM126A using MACS to obtain TTC7B-FAM126A specific nanobody (named F3IN).

(C) Size exclusion chromatography traces and corresponding SDS-PAGE gels of F3IN, TTC7B-FAM126A and chimeric TTC7B-EFR3A-FAM126A.

266 (D) Cartoon of BLI experiment with F3IN on the tip and TTC7B-FAM126A or TTC7B-chimera
267 EFR3A-FAM126A in solution. BLI traces of F3IN against TTC7B-FAM126A and chimeric TTC7B-
268 EFR3A-FAM126A.
269 (E) Cartoon of BLI experiment with F3IN on the tip and TTC7B-FAM126A in solution. Raw BLI
270 traces of F3IN (100 nM) binding to TTC7B-FAM126A (5 nM, 10 nM, 15 nM). The K_D was
271 calculated using a 1:1 binding model.
272 (F) Raw BLI traces for the binding of F3IN (100 nM) to TTC7B-FAM126A (50 nM) and TTC7B-
273 FAM126B (15 nM). The K_D was calculated using a 1:1 binding model.
274 (G) Raw BLI traces for the binding of F3IN (100 nM) to TTC7B-FAM126A (15 nM) and TTC7A-
275 FAM126A (15 nM). The K_D was calculated using a 1:1 binding model.
276 (H) Cartoon (L) of the BLI experiment. Raw BLI traces of F3IN (100 nM) binding to PI4KA-TTC7B-
277 FAM126A (2.5 nM, 5 nM, 10 nM). The K_D was calculated using a 1:1 binding model.
278 (I) Raw BLI traces for the binding of F3IN (100 nM) to PI4KA-TTC7B-FAM126A (5 nM) and PI4KA-
279 TTC7A-FAM126A (5 nM). The K_D was calculated using a 1:1 binding model.
280

281 ***Cryo-EM analysis of F3IN bound to PI4KA-TTC7B-FAM126A***

282 To identify the binding interface of F3IN with the PI4KA complex, we generated a
283 3D reconstruction of the PI4KA-TTC7B-FAM126A-F3IN nanobody complex, using cryo-
284 EM, at a nominal resolution of 3.54 Å (from 282,982 particles **(Fig 5A-B, S2A-F, Table**
285 **S2)**. Samples for cryo-EM analysis were prepared by brief treatment with a crosslinker to
286 stabilize the PI4KA complex, and similar to our previous cryo-EM analysis of PI4KA
287 regulatory complexes (11, 34). Using a combination of manual model building and
288 AlphaFold3 (35), we were able to generate a molecular model of F3IN binding to the
289 PI4KA-TTC7B-FAM126A trimer with the density allowing for manual building of the CDR
290 loops mediating interaction with the trimer **(Fig S2G)**. Local masked refinement centered
291 on the F3IN-TTC7B interface enabled unambiguous determination of the residues
292 mediating the interaction between F3IN and the PI4KA complex. The structure revealed
293 that F3IN included an additional extended beta strand within the CDR3 loop, which orients
294 it into the cavity normally occupied by the α3 helix of EFR3A **(Fig 5C-D)**. This orientation

295 suggests that F3IN sterically blocks EFR3A binding by occluding its binding with the
296 CDR3 loop.

297 The TTC7B-F3IN interface is composed of 415 $Å^2$ buried surface area. The
298 interface is mainly mediated by three TTC7B α helices, spanning residues 535-545, 546-
299 563, and 564-578. These helices interact directly with the extended β-strand in CDR3 of
300 F3IN. Although TTC7A and TTC7B have a sequence similarity of 49.7% with a highly
301 conserved C-terminus. Our structure revealed possible insight for why F3IN was
302 selective to TTC7B containing heterodimers. The most prominent difference is a glycine
303 residue in TTC7B (G546) that is not conserved in TTC7A, where it is replaced by a lysine
304 (K563). In the cryo-EM structure, G546 lies in close spatial proximity to R105 in the CDR3
305 of F3IN. This positioning suggests that the corresponding lysine in the TTC7A isoform
306 would result in a charge-charge repulsion with R105, potentially preventing nanobody
307 binding. Intriguingly, F3IN also interacts with the N-terminus of PI4KA resulting in 280 $Å^2$
308 of buried surface area. This interface is mediated by the N-terminus of F3IN and the N-
309 terminal horn of PI4KA, comprising a β-strand (residues 67-73) and a loop (residues 58-
310 66). This additional interface likely explains the increased affinity of F3IN with the PI4KA
311 complex, and why there was weak affinity for the PI4KA-TTC7A-FAM126A complex, but
312 not the TTC7A-FAM126A dimer.

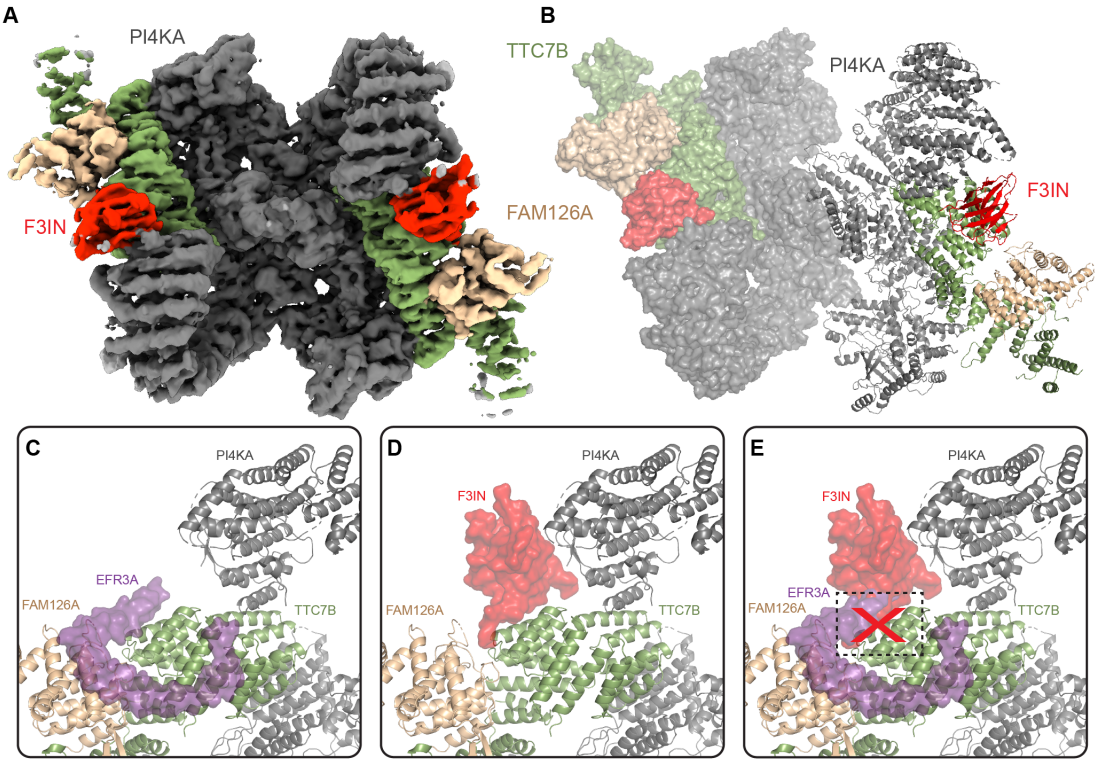

Figure 5. Cryo-EM analysis of F3IN binding to the PI4KA complex

(A) Cryo-EM density map of the PI4KA complex bound to F3IN.

(B) Molecular model of F3IN bound at the interface of TTC7B and the PI4KA horn domain.

(C) Zoomed in cartoon of the C terminus of EFR3A bound to the PI4KA complex. PDB: 9BAX)

(D) Zoomed in cartoon of F3IN bound at the interface of TTC7B and PI4KA.

(E) Overlay of the PI4KA-EFR3A (PDB: 9BAX) and PI4KA-F3IN models depicting binding of F3IN and EFR3A at the same TTC7B helix (represented as a black box with a red cross).

HDX-MS validation of epitopes on PI4KA and TTC7B

To further understand the dynamics of the interaction between PI4KA and F3IN, and we used HDX-MS on the PI4KA complex and PI4KA-F3IN complex. HDX-MS is a powerful technique to identify binding epitopes and investigate dynamic conformational changes. It measures the exchange of backbone amide hydrogens with deuterium (36, 37), with the rate of exchange being primarily dependent on secondary structure (38). HDX-MS experiments were performed comparing the PI4KA-TTC7B-FAM126A complex

329 alone and PI4KA-TTC7B-FAM126A complex bound to F3IN. We incubated the samples
330 with D_2O buffer at 4 different timepoints (3s, 30s, 300s, 3000s at 18^oC) with significant
331 differences between the two conditions defined as changes >0.4 Da, 5% at any given
332 time point and an unpaired t-test value of $p<0.01$. Upon F3IN binding, we observed a
333 significant decrease in deuterium incorporation at the N-terminus of the PI4KA horn in the
334 region 51-83 **(Fig. 6A-C)**, showing a clear epitope on PI4KA and supporting our cryo-EM
335 model. Surprisingly, we saw no clear decrease in exchange on TTC7B and instead
336 observed an increase in HDX in 539-545 in TTC7B.

337 In the absence of PI4KA, the TTC7B-FAM126A dimer also showed F3IN binding
338 with high affinity, therefore we wanted to determine whether there were conformational
339 differences of the nanobody binding to the dimer. We used HDX-MS to map the epitope
340 and investigate the differences in conformational dynamics of TTC7B-FAM126A upon
341 F3IN binding. HDX-MS experiments were performed to compare TTC7B-FAM126A in the
342 presence and absence of F3IN at 5 different timepoints (3, 30, 300, 3000, 1000s at 18^oC).
343 We observed a significant decrease in TTC7B in the peptide 539-544 consistent with the
344 interface observed in our cryo-EM analysis. We also measured a significant increase in
345 HDX in the subsequent peptide 545-554 **(Fig. 6D-F)**. Overall, this suggests that nanobody
346 binding induces a shift in dynamics in TTC7B, which may provide another mechanism for
347 selectivity compared to TTC7A.

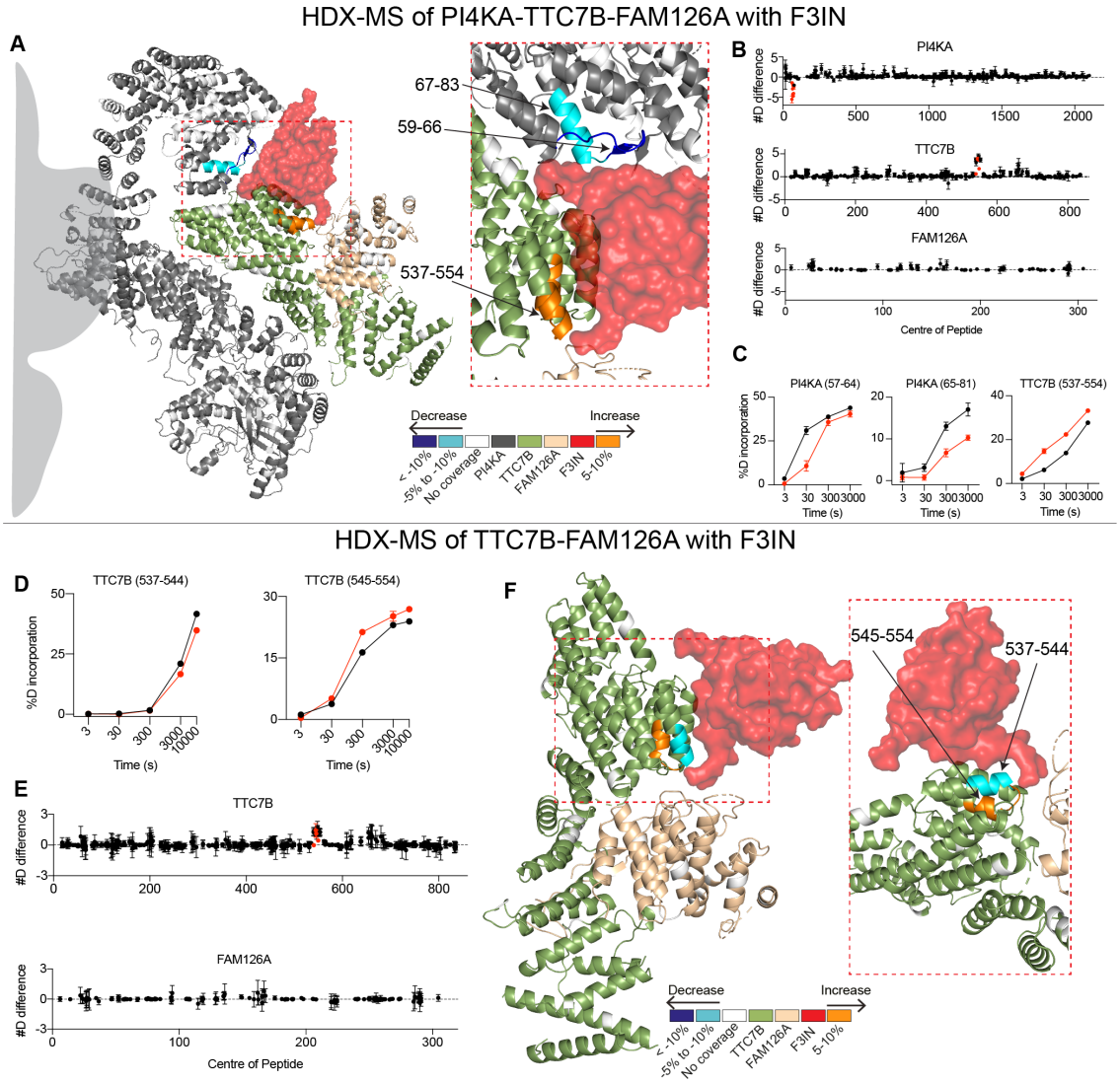

Figure 6. HDX-MS analysis of the interaction of F3IN with PI4KA and TTC7B

(A) HDX differences (significance defined as >5%, 0.4 Da, and P< 0.01 in an unpaired two-tailed t test at any time point) upon PI4KA complex binding to F3IN mapped on PI4KA-F3IN structure.

(B) Sum of the deuteron difference of the PI4KA complex upon binding to F3IN across the entire time course. Each point represents a single peptide. Peptides that met the significance criteria described in (A) are colored red. Error is shown as the sum of SDs across all time points (n=3).

(C) % Deuterium incorporation in PI4KA peptides showing significant changes in the presence (red) and absence (black) of F3IN.

(D) % Deuterium incorporation in TTC7B peptides showing significant changes in the presence (red) and absence (black) of F3IN.

359 (E) Sum of the deuteron difference of TTC7B-FAM126A upon binding to F3IN across the entire
360 time course. Peptides that met the significance criteria described in (A) are colored red. Error is
361 shown as the sum of SDs across all time points (n=3).
362 (F) HDX differences upon TTC7B-FAM126A binding to F3IN mapped on PI4KA-F3IN structure.

363

364 ***Nanobody F3IN competitively inhibits EFR3A binding***

365 The cryo-EM structure and HDX-MS results indicated that F3IN forms a dual
366 interface with both TTC7B and PI4KA. To investigate whether F3IN is a competitive
367 inhibitor of EFR3 for the TTC7B binding site, we developed a competition BLI assay.
368 Here, F3IN was loaded onto the biosensor and dipped into solution containing either 50
369 nM of TTC7B-FAM126A or 50 nM of TTC7B-FAM126A with increasing concentrations of
370 EFR3A (15 nM to 240 nM). We found that EFR3A robustly inhibited the binding of F3IN
371 to TTC7B-FAM126A until saturation at 240 nM of EFR3A **(Fig. 7A)**. This indicates that
372 both EFR3A and F3IN compete for the same binding site on TTC7B validating the cryo-
373 EM and HDX-MS analysis.

374 However, due to the unexpected interaction of F3IN with the horn region of PI4KA,
375 it was important to perform a BLI competition assay with the full PI4KA complex to
376 determine the degree of inhibition with the physiologically relevant complex. In this assay,
377 we used the same above-mentioned conditions with 10 nM PI4KA rather than the TTC7B-
378 FAM126A dimer. As expected, we observed a decrease in F3IN-PI4KA binding with
379 increasing concentration of EFR3A until saturation at 240 nM of EFR3A **(Fig. 7B)**.
380 Altogether, these results indicate that the F3IN nanobody competes with EFR3A for
381 binding to TTC7B and further validates its usefulness as a tool to specifically inhibit
382 TTC7B containing complexes of PI4KA.

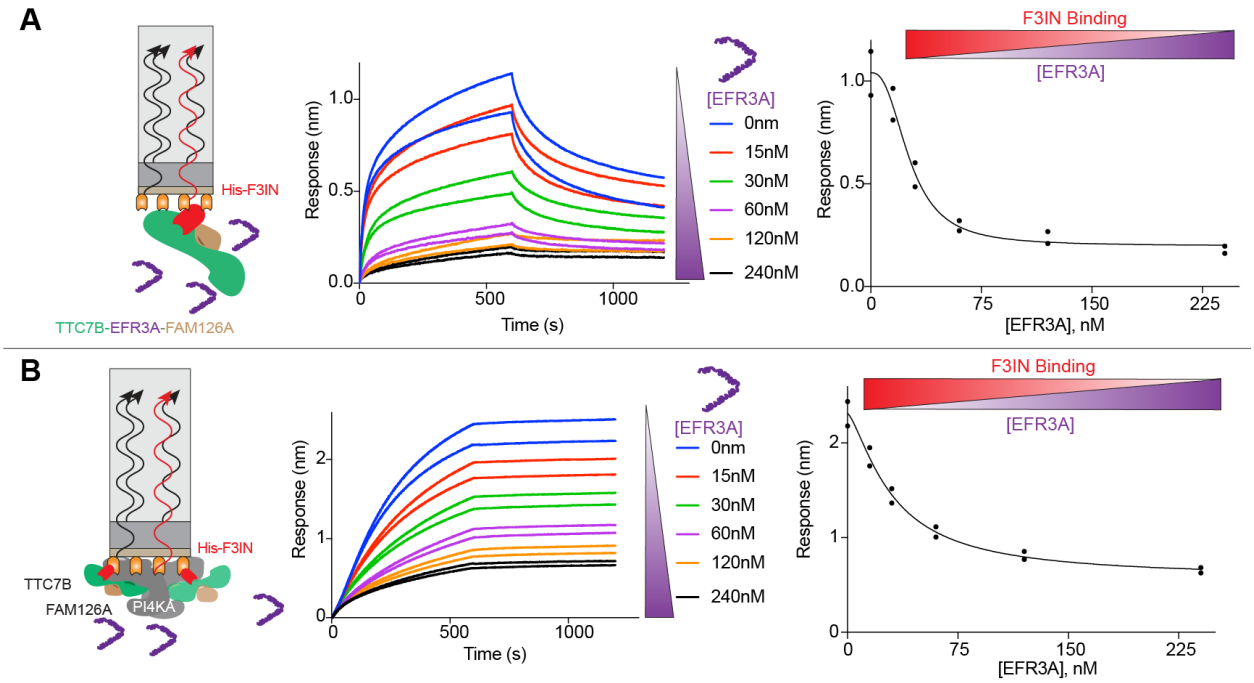

Figure 7. EFR3A competitively inhibits binding to F3IN for both the TTC7B-FAM126A dimer and the PI4KA-TTC7B-FAM126A trimer

(A) Cartoon (L) of BLI experiment with immobilized F3IN dipping into TTC7B-FAM126A solution with increasing concentrations of EFR3A. Raw association and dissociation curves (M) for the binding of F3IN (100 nM) to TTC7B-FAM126A (50 nM) at varying concentrations of EFR3A. (R) Dose response curve showing decrease in F3IN binding upon increase in EFR3A concentrations. (B) Cartoon (L) of BLI experiment with immobilized F3IN dipping into PI4KA complex solution with increasing concentrations of EFR3A. Raw association and dissociation curves (M) for the binding of F3IN (100 nM) to PI4KA complex (10 nM) at varying concentrations of EFR3A. (R) Dose response curve showing decrease in F3IN binding upon increase in EFR3A concentrations.

Discussion

Dysregulation of PI4KA and its regulatory partners is involved in multiple human diseases, arising from both gain- and loss-of-function alterations in PI4KA and its accessory proteins EFR3A, TTC7A, and FAM126A. The isoforms TTC7A/B, FAM126A/B, and EFR3A/B are widely expressed, however, there are distinct tissues that show enrichment for specific variants. Clinical mutations in several PI4KA accessory proteins have been identified. For example, patient-derived mutations in TTC7A result in severe intestinal developmental disorders and immunological deficiencies (17), and mutations in

403 FAM126A lead to hypomyelination and congenital cataract (9). However, no diseases are
404 yet known to be caused by mutations in TTC7B and FAM126B. Although the structure of
405 the C-terminus of EFR3A bound to the PI4KA-TTC7B-FAM126A complex (11) revealed
406 the possibility for distinct association between EFR3 with TTC7-FAM126 isoforms,
407 determining the differences in recruitment of different PI4KA complexes by EFR3 to the
408 PM remained important for defining potential isoform-specific roles. Here we find that
409 most EFR3 isoforms bind to most TTC7-FAM126 complexes with similar affinity (~0.3
410 nM), with the excpetion of EFR3A, which binds with a significantly higher affinity as its
411 interaction with TTC7B-FAM126A had a very slow k_{off} rate. This enhanced affinity for one
412 isoform complex may indicate a more stable PI4KA PM membrane recruitment and
413 activation, and could be important for PI4KA regulatory subunit specific signaling.

414 The C-terminus of EFR3 has 67% sequence identity between EFR3A and EFR3B.
415 There is differential expression of these isoforms, as EFR3A is highly expressed in testis,
416 fibroblasts, and adipocytes, and EFR3B is enriched in the brain and eye, and its
417 expression in fibroblasts and adipocytes is 30- to 100-fold lower than EFR3A (39, 40).
418 This differential expression suggests distinct tissue specific physiological roles for the two
419 isoforms. The N-terminus of the EFR3 proteins can be palmitoylated at cysteine residues,
420 with a palmitoylation code governing the spatial organisation at the PM (41, 42), further
421 diversifying their regulatory potential. Phosphorylation of Efr3 in yeast disrupts Stt4/Ypp1
422 (orthologs of PI4KA/TTC7) membrane recruitment, and therefore Stt4 activity (29).
423 Similarly, multiple phosphorylation sites map on mammalian EFR3A and EFR3B at the
424 TTC7-FAM126 interface. The location of these sites is divergent between the two
425 isoforms, suggesting other possible isoform-specific regulation of PI4KA complexes. We
426 determined *in vitro* phosphorylation of EFRB-Y723 by the Src family tyrosine kinase, LCK,
427 markedly decreased binding with TTC7B-FAM126A. However, determining whether this
428 is the physiological kinase requires further work, whilst also underscoring the need to
429 screen other Src family kinases as potential regulators of EFR3B, and, by extension,
430 regulators of PI4KA activity. Interestingly, Y723 in EFR3B is not conserved in EFR3A,
431 which instead contains a phenylalanine at the corresponding position (F728). This

432 divergence suggests a potential mechanism for differential regulation of the PI4KA
433 complex, possibly influenced by the distinct expression patterns and tissue specificity of
434 EFR3 isoforms. There is precedence for this type of regulation as phosphorylation of
435 EFR3A at S738 by serine/threonine kinases may modulate binding to TTC7B-FAM126A,
436 however, its impact on affinity remains unclear. The top ranked kinase for this site is polo
437 like kianse 1 (PLK1), which plays an important role in regulating cell division. Therefore,
438 phosphorylation of EFR3A may similarly play an important role in controlling PI4KA
439 membrane recruitment and activity. Further investigation on how EFR3 phosphorylation
440 is controlled in cells by the specific kinases and phosphatases will be key to
441 understanding PI4KA regulation.

442 Although the TTC7 isoforms are broadly expressed in mammals, there are key
443 differences. While TTC7B is expressed predominantly in the brain, TTC7A is highly
444 expressed in the gut and thymus with loss-of-function mutations in TTC7A causing severe
445 gastrointestinal diseases (17). Many of these mutations, including S539L, A551D, and
446 H570R, reside in helices that either bind the α3-helix of EFR3A or pack against the
447 interfacial helices. These diseases, caused by lack of PI4KA function, shed insight for
448 why PI4KA inhibitors have severe toxicity in animal models (26). Recently, it has been
449 proposed that PI4KA inhibitors may have a therapeutic window for treating some cancers
450 when used in combination with PI3K- or RAS-targeting inhibitors (23, 24). We
451 demonstrated that both PI4KA complexes are equally sensitive to established PI4KA
452 inhibitors, while simeprevir, which was previously reported as a direct inhibitor of PI4KA
453 (24, 32), showed no inhibitory activity, even at high concentrations. While opportunities
454 may still exist for using PI4KA inhibitors, the development of isoform-specific
455 biomolecules offer a more refined approach. We reason that blocking EFR3 mediated
456 plasma membrane recruitment of PI4KA could represent a useful approach to regulate
457 its activity. Indeed, modulating PI4KA activity, without fully inhibiting it, could potentially
458 reveal a novel therapeutic strategy .

459 In recent years, nanobodies have emerged as tools in stabilizing and disrupting
460 protein-protein interactions (43). For example, nanobodies binding to the spike protein of

461 SARS-CoV2 alter its conformational dynamics disrupting binding with host receptors (44).
462 Similarly, in the context of RAS signaling, nanobodies bind to SOS1 and competitively
463 inhibits SOS1-RAS signaling (45). Therefore, there is sufficient evidence for the use of
464 the nanobodies as complex disruptors. Using a yeast display approach, we isolated and
465 characterized a nanobody we called F3IN that binds specifically to TTC7B and
466 competitively inhibits the EFR3-TTC7B interaction. Our cryo-EM and HDX-MS analyses
467 showed that F3IN binds at the interface of PI4KA and TTC7B and induced a
468 conformational change in TTC7B upon binding. The specificity of F3IN for TTC7B is of
469 particular importance in TTC7B-enriched tissues, as EFR3A has stronger affinity for this
470 isoform compared to TTC7A. From a physiological perspective, the ability to selectively
471 inhibit EFR3 mediated PI4KA recruitment will provide additional insight on PI4KA
472 regulation. Future experiments will need to address the functional role of blocking EFR3
473 mediated PI4KA recruitment in specific tissues in vivo.

474 In conclusion, our study provides a detailed molecular framework for
475 understanding isoform-specific regulation of PI4KA and introduces a nanobody-based
476 approach to selectively modulate PI4KA membrane recruitment. These findings lay the
477 foundation for future efforts aimed at the development of more targeted, less toxic
478 strategies to modulate PI4KA function in disease.
479

480 **Experimental procedures**

481 ***Plasmids***

482 Plasmids containing genes for full-length SSH-PI4KA-TTC7B-FAM126A (1-308) were
483 cloned into the MultiBac vector, pACEBac1 (Geneva Biotech) as described in (8).
484 Plasmids containing genes for full-length SSH-PI4KA-TTC7A-FAM126A (1-308), SSH-
485 TTC7A-FAM126A, and SSH-TTC7A-FAM126B were cloned in the pBIG1a biGBac vector
486 using the biGbac cloning method (46). Final pACEbac1 and pBIG1a constructs were
487 transformed into DH10EmBacY cells (Geneva Biotech), with white colonies indicating
488 successful generation of bacmids containing our genes of interest. Plasmid encoding

489 TTC7B and FAM126A (1 to 308) was subcloned into a pOPT vector containing an N-
490 terminal 10x histidine tag, followed by a 2x Strep tag, followed by a tobacco etch virus
491 (TEV) protease cleavage site (47). EFR3A (721 to 791) was subcloned into a pOPT
492 vectors containing an N-terminal MBP tag in addition to the 10x histidine tag and 2x Strep
493 tag. Nanobody F3IN was cloned into the pET22b vector for inducible expression in the
494 periplasm.

495 ***Protein Expression***

496 Plasmid containing the coding sequences for MBP-EFR3A (721-791) was expressed in
497 BL21 DE3 C41 *Escherichia coli* and induced with 0.5 mM IPTG and grown at 37 °C for
498 4 h. The TTC7B-FAM126A (1-308), TTC7B-FAM126B (1-308) and chimeric TTC7B-
499 EFR3A-FAM126A constructs were expressed in BL21 DE3 C41 cells and induced with
500 0.1mM IPTG and grown at 21 °C for 20 hours. The F3IN construct was expressed in BL21
501 DE3 C41 cells and induced with 1mM IPTG and grown at 25°C for 20 hours. Cells were
502 then harvested and centrifuged at 15,000*g*. Pellets were washed with PBS before being
503 snap-frozen in liquid nitrogen, followed by storage at –80 °C.

504 Bacmid harboring TTC7A-FAM126A (1-308), TTC7A-FAM126B (1-308), PI4KA-
505 TTC7B-FAM126A (1-308) and PI4KA-TTC7A-FAM126A (1-308) were transfected into
506 *Spodoptera frugiperda (Sf9) cells*, and viral stocks amplified for one generation to acquire
507 a P2 generation final viral stock. Final viral stocks were added to *Sf9* cells in a 1/100 virus
508 volume to cell volume ratio. Constructs were expressed for 65-72 hours before harvesting
509 of the infected cells. Cell pellets were washed with PBS, flash frozen in liquid nitrogen,
510 and stored at –80 °C.

511 ***Protein Purification***

512 *F3IN purification:* Nanobody F3IN was isolated from cell pellets by osmotic shock. Cell
513 pellets were resuspended in 20 ml of TES buffer (0.2 M Tris pH 8.0, 0.5 mM
514 ethylenediaminetetraacetic acid (EDTA), 0.5 M sucrose) with Protease Inhibitor Cocktail
515 Set III and rotated for 45 min at 4°C. Twice the volume of TES/4 buffer was added to the
516 cells and rotated for 45 min at 4°C, followed by centrifugation at 14,000 rpm for 20 min at

517 4°C in a JA-20 rotor. The periplasmic extract was loaded onto a His-Trap HP column
518 (Cytiva) equilibrated with Ni–NTA A buffer (20 mM Tris [pH 8.0], 100 mM NaCl, 20 mM
519 imidazole [pH 8.0], 5% [v/v] glycerol, and 2 mM βME). The column was washed with 4
520 CV of high salt buffer (20 mM Tris [pH 8.0], 1 M NaCl, 5% [v/v] glycerol, and 2 mM bME),
521 then 3-4 CV of Ni–NTA A buffer, followed by 3-4 CV of 6% Ni–NTA B buffer (20 mM Tris
522 [pH 8.0], 100 mM NaCl, 200 mM imidazole [pH 8.0], 5% [v/v] glycerol, and 2 mM bME)
523 before being eluted with 3-4 CV of 100% Ni–NTA B buffer. The protein elution was then
524 buffer exchanged into PI4KA GFB (20 mM Imidazole [pH 7.0], 150 mM NaCl, 5% [v/v]
525 glycerol and 0.5 mM Tris (2-carboxyethyl) phosphine (TCEP) and concentrated in a 10
526 kDa MWCO concentrator (Millipore Sigma). The concentrated protein was loaded onto
527 the Superdex 75 Increase 10/300 GL (Cytiva) pre-equilibrated in GFB. Protein fractions
528 were collected and concentrated in a 10 kDa MWCO concentrator (Millipore Sigma), flash
529 frozen in liquid nitrogen, and stored at –80 °C.

530 *MBP-EFR3A purification:* Cell pellets were lysed by sonication for 5 min in lysis
531 buffer (20 mM Tris [pH 8.0], 100 mM NaCl, 5% [v/v] glycerol, 20 mM imidazole, 2 mM β-
532 mercaptoethanol [bME]), and protease inhibitors [Millipore Protease Inhibitor Cocktail Set
533 III, EDTA free]). Triton X-100 was added to 0.1% v/v, and the solution was centrifuged for
534 45 min at 20,000*g* at 1 °C (Beckman Coulter J2-21, JA-20 rotor). The supernatant was
535 then loaded onto a 5 ml HisTrap column (Cytiva) that had been equilibrated in nickel–
536 nitrilotriacetic acid (Ni–NTA) A buffer (20 mM Tris [pH 8.0], 100 mM NaCl, 20 mM
537 imidazole [pH 8.0], 5% [v/v] glycerol, and 2 mM βME). The column was washed with 4
538 CV of high salt buffer (20 mM Tris [pH 8.0], 1 M NaCl, 5% [v/v] glycerol, and 2 mM βME),
539 then 3-4 CV of Ni–NTA A buffer, followed by 3-4 CV of 6% Ni–NTA B buffer (20 mM Tris
540 [pH 8.0], 100 mM NaCl, 200 mM imidazole [pH 8.0], 5% [v/v] glycerol, and 2 mM βME)
541 before being eluted with 3-4 CV of 100% Ni–NTA B. The eluate was then loaded onto a
542 5 ml StrepTrapHP column (Cytiva) and washed with 3-4 CV of high salt gel filtration buffer
543 (GFB) (20 mM HEPES [pH 7.5], 500 mM NaCl, 5% [v/v] glycerol and 1 mM Tris(2-
544 carboxyethyl) phosphine [TCEP]), then 1 CV of GFB containing 2 mM ATP, 10 mM $MgCl_2$,
545 and 150 mM KCl, followed by 4 CV of GFB (20 mM HEPES [pH 7.5], 150 mM NaCl, 5%

546 [v/v] glycerol and 1 mM Tris (2-carboxyethyl) phosphine [TCEP]). Protein was eluted with
547 3 CV of GFB containing 2.5 mM desthiobiotin and concentrated in a 10 kDa MWCO
548 concentrator (Millipore Sigma). Concentrated protein was loaded onto the Superdex 75
549 Increase 10/300 GL (Cytiva) or the Superdex 200 Increase 10/300 GL (Cytiva) pre-
550 equilibrated in GFB. Protein fractions were collected and concentrated in a 10 kDa
551 MWCO concentrator (Millipore Sigma), flash frozen in liquid nitrogen, and stored
552 at –80 °C.

553 *TTC7-FAM126 (1-308) purification:* Cell pellets were lysed by sonication for 5 min
554 in lysis buffer (20 mM imidazole [pH 8.0], 100 mM NaCl, 5% [v/v] glycerol, 2 mM bME),
555 and protease inhibitors [Millipore Protease Inhibitor Cocktail Set III, animal-free]. Triton
556 X-100 was added to 0.1% v/v, and the solution was centrifuged for 45 min at 20,000*g* at
557 1 °C. The supernatant was then loaded onto a 5 ml HisTrap column (Cytiva) that had
558 been equilibrated in nickel–nitrilotriacetic acid (Ni–NTA) A buffer (20 mM Tris [pH 8.0],
559 100 mM NaCl, 20 mM imidazole [pH 8.0], 5% [v/v] glycerol, and 2 mM βME). The column
560 was washed with 3-4 CV Ni-NTA A buffer (20 mM imidazole [pH 8.0], 100 mM NaCl, 5%
561 [v/v] glycerol, and 2 mM βME) followed by 3-4 CV of 6% Ni–NTA B buffer (450 mM
562 Imidazole [pH 8.0], 100 mM NaCl, 5% [v/v] glycerol, and 2 mM βME) before being eluted
563 with 3-4 CV of 100% Ni–NTA B. The eluate was then loaded onto a 5 ml StrepTrapHP
564 column (Cytiva) and then washed with 3-4 CV of GFB (20 mM Imidazole [pH 7.0], 150 mM
565 NaCl, 5% [v/v] glycerol and 0.5 mM Tris (2-carboxyethyl) phosphine (TCEP)). The His-
566 strep tag was cleaved with tobacco etch virus protease containing a stabilizing lipoyl
567 domain (Lip-TEV). TEV cleavage proceeded overnight following which the protein was
568 eluted with GFB. Protein eluate was further concentrated in a 50 kDa MWCO concentrator
569 (Millipore Sigma). Concentrated protein was loaded onto the Superdex 200 Increase
570 10/300 GL (Cytiva) or the Superose 6 Increase 10/300 GL (Cytiva) pre-equilibrated in
571 GFB. Protein fractions from a single peak were collected and concentrated in 50 kDa
572 MWCO concentrator (Millipore Sigma), flash frozen in liquid nitrogen and stored at -80 °C
573 until further use.

574 *PI4KA-TTC7B-FAM126A (1-308) purification*: Sf9 pellets were resuspended in
575 lysis buffer [20 mM imidazole pH 8.0, 100 mM NaCl, 5% glycerol, 2 mM βMe, protease
576 (Protease Inhibitor Cocktail Set III, Sigma)] and lysed by sonication. Triton X-100 was
577 added to 0.1% v/v final, and lysate was centrifuged for 45 min at 20,000×g at 1 °C. The
578 supernatant was then loaded onto a 5 ml HisTrap column (Cytiva) that had been
579 equilibrated in nickel–nitrilotriacetic acid (Ni–NTA) A buffer (20 mM Tris [pH 8.0], 100 mM
580 NaCl, 20 mM imidazole [pH 8.0], 5% [v/v] glycerol, and 2 mM bME). The column was
581 washed with 3-4 CV of Ni-NTA A buffer (20 mM imidazole [pH 8.0], 100 mM NaCl, 5%
582 [v/v] glycerol, and 2 mM βME) followed by 3-4 CV of 6% Ni–NTA B buffer (27 mM
583 Imidazole [pH 8.0], 100 mM NaCl, 5% [v/v] glycerol, and 2 mM βME) before being eluted
584 with 3-4 CV of 100% Ni–NTA B. Eluted protein was loaded onto a 5 ml StrepTrapHP
585 column (Cytiva) pre-equilibrated GFB (20 mM imidazole pH 7.0, 150 mM NaCl, 5%
586 glycerol [v/v], 0.5 mM TCEP). The His-strep tag was cleaved with Lip-TEV, and cleavage
587 proceeded overnight. Cleaved protein was eluted with GFB and concentrated in a 50 kDa
588 MWCO concentrator (MilliporeSigma). Concentrated protein was loaded onto the
589 Superose 6 Increase 10/300 GL (Cytiva) pre-equilibrated in GFB. Protein fractions from
590 a single peak were collected and concentrated in 50 kDa MWCO concentrator (Millipore
591 Sigma), flash-frozen in liquid nitrogen and stored at -80 °C until further use.
592 The raw SDS-PAGE gel images for all purified proteins are shown in the source
593 data.

594 **Phosphorylation analysis**

595 For the phosphorylation of EFR3B, (20 μM) of protein was mixed with 1mM of ATP, 5mM
596 of $MgCl_2$, and 13 ug of LCK kinase. An unphosphorylated control containing equivalent
597 amount of GFB (20 mM HEPES [pH 7.5], 150 mM NaCl, 5% [v/v] glycerol and 0.5 mM
598 TCEP) instead of LCK kinase was also prepared. Reactions were incubated overnight on
599 ice at 4°C. Subsequently, the protein mixtures were loaded onto a Superdex 200 10/300
600 GL (Cytiva) pre-equilibrated in GFB. Protein fractions from a single peak were collected
601 and concentrated in 30 kDa MWCO concentrator (Millipore Sigma), flash-frozen in liquid
602 nitrogen and stored at -80 °C until further use.

603 Phosphorylation of all proteins was confirmed using mass spectrometry and FragPipe
604 v18.0 analysis. The LC-MS analysis of these samples was carried out using the same
605 pipeline as used in the HDX-MS section below. The phosphorylated and non-
606 phosphorylated peptide ratios were determined by generating extracted ion
607 chromatograms (EIC) in the Thermo Xcalibur qual browser. The full analysis with EIC and
608 MS data is provided in the source data.

609 ***Lipid Vesicle Preparation***

610 For inhibitor response assays of the PI4KA complexes, lipid vesicles containing 100% PI
611 were prepared by mixing the lipid dissolved in organic solvent. The solvent was
612 evaporated in a stream of argon following which the lipid film was desiccated in a vacuum
613 for 1 hour. The lipids were resuspended in lipid buffer (20 mM HEPES pH 7.5, 100 mM
614 KCl and 0.5 mM EDTA) and the solution was sonicated for 15 minutes. The vesicles were
615 subjected to ten freeze thaw cycles and passed through an extruder (Avanti Research)
616 with a 100 nm filter 21 times. The extruded vesicles were aliquoted and stored at –80°C.

617 ***Lipid Kinase Assays***

618 All lipid kinase activity assays employed the Transcreener ADP2 Fluorescence Intensity
619 (FI) Assay (Bellbrook labs) which measures ADP production. For assays measuring
620 inhibitor response, the final concentration of 100% PI vesicles was 0.25 mg/mL, ATP was
621 100 µM ATP and inhibitors were 10 µM, 2 µM, 400 nM, 80 nM, 16 nM, or 3.2 nM (GSK-
622 A1 only) (1% DMSO final). Two µL of PI4KA complex solution at 2X final concentration
623 (10 nM final) was mixed with 2 µL substrate solution containing ATP, vesicles and
624 inhibitors and the reaction was allowed to proceed for 60 min at 20°C. The reaction was
625 stopped with 4 µL of 2X stop and detect solution containing Stop and Detect buffer, 8 nM
626 ADP Alexa Fluor 594 Tracer and 93.7 µg/mL ADP2 Antibody IRDye QC-1 and incubated
627 for 60 minutes. The fluorescence intensity was measured using an Agilent BioTek
628 synergy H1 plate reader at excitation 585 nm and emission 626 nm. This data was
629 normalised against a 0–100% ADP window made using conditions containing either 100
630 µM ATP or ADP with kinase buffer.

631 ***Isolation of nanobodies from the yeast surface display library***

632 The nanobodies were isolated from a yeast display library obtained from Dr. A.C.
633 Kruse's laboratory at Harvard Medical School and described in (48). The detailed
634 protocol to isolate nanobodies from the yeast display library can be obtained from the
635 Kruse laboratory website at:
636 (https://kruse.hms.harvard.edu/sites/kruse.hms.harvard.edu/files/files/Nanobody_protoc
637 ol_0.pdf)

638 The yeast cultures were grown in a selective dropout medium without tryptophan
639 at 30°C. Nanobody expression was induced before each step by growing the cells in a
640 dropout medium without tryptophan and with 2% galactose at 25°C for 48 to 72 hours.
641 The library screening involved two rounds of magnetic-activated cell sorting (MACS)
642 followed by two rounds of fluorescence-activated cell sorting (FACS) and a final round of
643 MACS with a counter-selection step. The protein antigens (TTC7B-FAM126A (1-308) or
644 chimeric TTC7B-EFR3A-FAM126A) were labelled using the Fluoreporter FITC protein
645 labeling kit (Invitrogen F6434), the AlexaFluor-488 antibody labeling kit (Invitrogen
646 A20181) or the Alexa Fluor 647 antibody labeling kit (Invitrogen A20186).

647 For MACS1, 1.1 x 10^{10} induced yeast cells were washed and re-suspended in
648 4.5ml selection buffer (20mM HEPES pH 7.5, 150mM sodium chloride, 0.1% (w/v) bovine
649 serum albumin, 5mM maltose) and incubated with 500µl anti-FITC microbeads (Miltenyi
650 130-048-701) at 4°C for 40 minutes. After incubation with the magnetic beads, the cells
651 were spun down and the excess unbound beads were removed with the supernatant. The
652 cells were then resuspended in buffer and passed through a LD column (Miltenyi 130-
653 042-901) to eliminate any yeast clones expressing nanobodies that bind non-specifically
654 to the magnetic beads. The flow through from the LD column was spun down and stained
655 in a solution of 1µM FITC-labelled TTC7B-FAM126A (1-308) in selection buffer for 1 hour
656 at 4°C, spun down and re-suspended in 4.5ml selection buffer and 500µl anti-FITC
657 microbeads, incubated for 20 minutes at 4°C and loaded on a LS column (Miltenyi 130-
658 042-401). The cells binding to the column were eluted and grown for the next round of
659 selection. The same protocol was used for the second round of MACS, except that we

660 started with 2.5 x 10^9 induced cells, the antigen was 38nM Alexa Fluor 647-labeled
661 TTC7B-FAM126A (1-308) and anti-Alexa Fluor 647 microbeads were used (Miltenyi 130-
662 091-395).

663 FACS selection was performed using a Cytoflex SRT cell sorter (Beckman
664 Coulter). The induced cells were labeled with 1:200 AF647-labeled anti-HA antibody
665 (Invitrogen 26183-A647) and 17nM FITC-labeled TTC7B-FAM126A (1-308) (FACS1) or
666 10nM AF488-labeled TTC7B-FAM126A (1-308) (FACS2) in selection buffer. Cells
667 staining for both fluorophores were collected.

668 A final round of magnetic selection (MACS3) was performed after FACS2 to enrich
669 for nanobodies that bind the TTC7B-FAM126A (1-308) at the EFR3A-binding interface.
670 1.5 x 10^8 induced cells were stained with 20nM AlexaFluor647-labeled chimeric TTC7B-
671 EFR3A-FAM126A and anti-AlexaFluor647 microbeads as described above and loaded
672 on a LD column. The flow through was collected and stained with 20nM AlexaFluor647-
673 labeled TTC7B-FAM126A (1-308) and anti-AlexaFluor647 microbeads and loaded on a
674 LS column. The cells bound to the column were eluted and plated to isolate single
675 colonies. The colonies were picked, grown and induced in a 96-well plate format for
676 analysis by flow cytometry using a Cytoflex instrument (Beckman Coulter). 2 x 10^6
677 induced cells from each colony were stained with 1:1000 AF488-anti-HA antibody to
678 monitor nanobody expression levels and either 10nM AF647-labeled TTC7B-FAM126A
679 (1-308) or 10nM AF647-labeled chimeric TTC7B-EFR3A-FAM126A. Clones that bound
680 well to the TTC7B-FAM126A (1-308) but not the chimeric TTC7B-EFR3A-FAM126A were
681 kept for subcloning and further analysis.

682 **Cryo-EM sample preparation and data collection**

683 The PI4KA complex and F3IN were thawed and mixed at a 1:3 molar ratio and left to
684 incubate on ice for 15 minutes. BS^3 crosslinker was added with a final concentration of
685 0.25 mM and left to incubate on ice for 15 minutes followed by the addition of TRIS pH 7
686 for a final concentration of 25 mM to quench the reaction and incubated on ice for at least
687 15 minutes. C-Flat 2/1-3Cu-T-50 grids were glow-discharged for 25 s at 15 mA using a

688 Pelco easiGlow glow discharger. 3 µL of the PI4KA complex and F3IN solution were
689 applied to the grids at 0.75 mg/mL and vitrified using a Vitrobot Mark IV (Thermo Fisher)
690 by blotting for 1.5 s at a blot force of –5 at 4°C and 100% humidity. Grids were screened
691 at the UBC High-Resolution Macromolecular Cryo-EM (HRMEM) facility on a 200kV
692 Glacios microscope (Thermo Fisher) equipped with a Falcon 3 camera (Thermo Fisher)
693 to determine suitability for further data collection. Data was collected at the UBC High-
694 Resolution Macromolecular Cryo-EM (HRMEM) facility on a 300kV Krios G2 microscope
695 (Thermo Fisher) equipped with a Falcon 4i camera (Thermo Fisher) and Selectris energy
696 filter (Thermo Fisher), using EPU software (Thermo Fisher). Data were collected at
697 165,000x magnification with a pixel size of 0.77 Å and a total dose of 50 $e^-/Å^2$, using a
698 defocus range of –0.5 to –2.0 µm.

699 **Cryo-EM image processing**

700 All data processing was carried out using cryoSPARC v4.5.2. Movies were imported with
701 default settings. Patch motion correction output F-crop factor set to 1/2 was applied to all
702 movies to align the frames. The contrast transfer function (CTF) of the resulting
703 micrographs was estimated using the patch CTF estimation job with default settings. Final
704 particle stack was manually curated to contain only micrographs with a CTF fit resolution
705 less than or equal to 10.

706 To generate initial 3D models, 587,975 particles were picked from 4021 micrographs
707 using a templates generated from a 3D reconstruction of the PI4KA complex from an
708 independent dataset (without F3IN) lowpass filtered to 20 Å. Particles were extracted with
709 a box size of 560 pixels and subjected to two rounds of 2D classification, removing
710 duplicate particles, with 40 online-EM iterations, to remove junk and ice contamination.
711 The resulting 69,526 particles underwent ab-initio reconstruction with two classes.

712 The complete dataset was then template picked as above (3,176,029 particles) and
713 inspected with the inspect pics job, removing particles picking ice contamination.
714 2,262,222 particles were extracted with a box size of 560 pixels and subjected to two
715 rounds of 2D classification with 40-online EM iterations. The remaining 657,836 particles

716 underwent heterogenous refinement using the two ab-initio reconstructions from the small
717 dataset. 329,699 particles from the class resembling the PI4KA complex underwent two
718 rounds of homogeneous refinement followed by particle orientation rebalancing
719 (rebalance percentile 80) prior to homogeneous refinement with C2 symmetry enforced.
720 282,982 particles then underwent C2 symmetry expansion followed by two rounds of
721 masked local refinement with a mask covering the entire molecule. This generated a
722 global reconstruction with an overall resolution of 3.54 Å based on the Fourier shell
723 correlation (FSC) 0.143 criterion. To improve the quality of the TTC7B-F3IN interface,
724 mask bases containing either TTC7B-NB-6C11 were generated in ChimeraX and
725 uploaded to cryoSPARC to generate masks used for masked local refinement and particle
726 subtraction. The masked local refinements had their fulcrums centered at the TTC7B-
727 F3IN interface, and generated refinements with an overall resolution of 3.66 Å (Local
728 Refinement A) and 3.77 Å (Local Refinement B) based on the Fourier shell correlation
729 (FSC) 0.143 criterion. A composite map was then generated using the global
730 reconstruction and local refinement A and B in ChimeraX. The local resolutions of the
731 three maps were determined with an FSC threshold of 0.143. The workflow to generate
732 the final cryo-EM map is shown in Fig S2.

733 ***HDX-MS sample preparation***

734 HDX reactions examining TTC7B-FAM126A (1-308) in the presence and absence of F3IN
735 were carried out in 10 μL reaction volumes containing 15 pmol of TTC7B-FAM126A (1.5
736 μM TTC7B-FAM126A) and 30 pmol of F3IN (3 μM F3IN in the bound state). The
737 exchange reactions were initiated by the addition of 8.4 μL of D_2O buffer (20 mM
738 Imidazole pH 7, 150 mM NaCl) to 1.6 μL of protein (final D_2O concentration of 78.9%
739 [v/v]). Reactions proceeded for 3s, 30s, 300s, 3000s, and 10,000s at 18°C before being
740 quenched with ice cold acidic quench buffer, resulting in a final concentration of 0.6M
741 guanidine HCl and 0.9% formic acid.

742 HDX reactions examining the PI4KA complex in the presence and absence of F3IN
743 were carried out in 10 μL reaction volumes containing 15 pmol of protein (1.5 μM PI4KA
744 complex, 1.5 μM F3IN in the bound state). The exchange reactions were initiated by the

745 addition of 7.5 μL of D_2O buffer (20 mM Imidazole pH 7, 150 mM NaCl) to 2.5 μL of protein
746 (final D_2O concentration of 70.2 % [v/v]). Reactions proceeded for 3s, 30s, 300s and
747 3000s, at 18°C before being quenched with ice cold acidic quench buffer, resulting in a
748 final concentration of 0.6M guanidine HCl and 0.9% formic acid post quench.

749 All conditions and timepoints were created and run in independent triplicate. All
750 samples were flash frozen immediately after quenching and stored at -80°C.

751 ***Protein digestion and MS/MS data collection***

752 Protein samples were rapidly thawed and injected onto an integrated fluidics system
753 containing a HDx-3 PAL liquid handling robot and climate-controlled (2°C)
754 chromatography system (Trajan), a Dionex Ultimate 3000 UHPLC system, as well as an
755 Impact HD QTOF Mass spectrometer (Bruker). The full details of the automated LC
756 system are described in (49). The TTC7B-FAM126A and PI4KA complex samples were
757 run over one immobilized pepsin column (Trajan; ProDx protease column, 2.1 mm x 30
758 mm PDX.PP01-F32) at 200 μL/min for 3 minutes at 10°C, and the F3IN samples were
759 run over two immobilized pepsin columns (Waters; Enzymate Protein Pepsin Column,
760 300Å, 5μm, 2.1 mm X 30 mm) at 350 μL/min for 3 minutes at 2°C. The resulting peptides
761 were collected and desalted on a C18 trap column (ACQUITY UPLC BEH C18 1.7mm
762 column (2.1 mm x 5 mm); Waters 186004629). The trap was subsequently eluted in line
763 with an ACQUITY 1.7 µm particle, 100 mm × 2.1 mm C18 UPLC column (Waters;
764 186003686), using a gradient of 3-35% B (Buffer A 0.1% formic acid; Buffer B 100%
765 acetonitrile) over 11 minutes immediately followed by a gradient of 35-80% over 5
766 minutes. Mass spectrometry experiments acquired over a mass range from 150 to 2200
767 m/z using an electrospray ionization source operated at a temperature of 200°C and a
768 spray voltage of 4.5 kV.

769 ***Peptide identification***

770 Peptides were identified from non-deuterated samples using data-dependent acquisition
771 following tandem MS/MS experiments (0.5s precursor scan from 150-2000 m/z; twelve
772 0.25s fragment scans from 150-2000 m/z). MS/MS datasets were analysed using

773 FragPipe v18.0 and peptide identification was carried out by using a false discovery-
774 based approach using a database of purified proteins and known contaminants (50, 51).
775 MSFragger was used, and the precursor mass tolerance error was set to -20 to 20ppm.
776 The fragment mass tolerance was set at 20ppm. Protein digestion was set as nonspecific,
777 searching between lengths of 4 and 50 aa, with a mass range of 400 to 5000 Da.

778 ***Mass Analysis of Peptide Centroids and Measurement of Deuterium Incorporation***

779 HD-Examiner Software (Sierra Analytics) was used to automatically calculate the level of
780 deuterium incorporation into each peptide. All peptides were manually inspected for
781 correct charge state, correct retention time, appropriate selection of isotopic distribution,
782 etc. Deuteration levels were calculated using the centroid of the experimental isotope
783 clusters. Results are presented as relative levels of deuterium incorporation, and the only
784 control for back exchange was the level of deuterium present in the buffer (78.9% or
785 70.2%). Differences in exchange in a peptide were considered significant if they met all
786 three of the following criteria: ≥5% change in exchange, ≥0.4 Da difference in exchange,
787 and a p value <0.01 using a two tailed student t-test. The entire HDX-MS dataset with all
788 the values and statistics are provided in the source data. Samples were only compared
789 within a single experiment and were never compared to experiments completed at a
790 different time with a different final D_2O level. The data analysis statistics for all HDX-MS
791 experiments are provided in the source data according to the guidelines of (52). The HDX-
792 MS proteomics data have been deposited to the ProteomeXchange Consortium via the
793 PRIDE (53) partner repository with the dataset identifier PXD066213.

794 ***Bio-layer interferometry (BLI)***

795 The BLI measurements were conducted using a Fortebio (Sartorius) K2 Octet using fiber
796 optic biosensors according to the protocols of (54). Anti–penta-His biosensors were
797 loaded using purified F3IN, which had a 6x His tag on the C-terminus. The biosensor tips
798 were preincubated in the BLI buffer (20 mM HEPES [pH 7.5], 150 mM NaCl, 0.01%,
799 bovine serum albumin, and 0.002% Tween-20) for 10 min before experiments began. The
800 sequence of steps in each assay was regeneration, custom, loading, baseline,

801 association, and dissociation. Every experiment was done at 25 °C with shaking at
802 1000 rpm. Technical replicates were performed by using the same fiber tip and repeating
803 the steps outlined previously. Regeneration was performed by exposing the tips to
804 regeneration buffer (Glycine pH 1.5) for 5s and BLI buffer for 5s and repeating the
805 exposure for 6 cycles. BLI buffer was used for the custom, baseline, and dissociation
806 steps; these steps were performed in the same well for a given sample. To determine
807 affinity constants, F3IN was diluted in BLI buffer to 100 nM and was loaded onto the anti
808 penta-His biosensor tips. TTC7B-FAM126A or PI4KA complex were also diluted in BLI
809 buffer and added to the appropriate association wells. Non-specific association was
810 controlled by loading 100 nM of His-MBP onto the biosensor tips and subtracting its
811 responses from the responses measured with F3IN. The data were fit to a 1:1 model
812 using the "full (assoc and dissoc) setting". Reported kinetic binding constants (K_D, K_{ON},
813 and K_{OFF}) values were calculated by taking the geometric mean of binding constants
814 calculated for individual conditions and replicates.

815 For the competition experiments, F3IN was diluted in BLI buffer to 100 nM and
816 TTC7B-FAM126A or PI4KA complex was diluted in BLI buffer to 50 nM or 10 nM
817 respectively. MBP-EFR3A was added to the association wells in increasing
818 concentrations (0, 15, 30, 60, 120, 240 nM). All BLI experiments were performed using
819 two technical replicates.

820

821 **Data availability**

822 The EM data have been deposited in the EM data bank with accession numbers EMD-
823 70826 (Composite map), EMD-70822 (Consensus map), EMD-70824 (Local Refinement
824 A map), and EMD-70825 (Local Refinement B map), and the associated structural model
825 has been deposited to the PDB with accession number (PDB: 9O6T) (Extended PDB ID:
826 pdb_00009O6T). The MS proteomics data have been deposited to the ProteomeXchange
827 Consortium via the PRIDE partner repository with the dataset identifier PXD066213 (53).
828 All raw data in all figures are available in the source data excel file. All data needed to

evaluate the conclusions in the paper are present in the paper and/or the supporting information.

Supporting information

This article contains supporting information.

Acknowledgements

Grids were prepared and data collected at the High Resolution Macromolecular Electron Microscopy (HRMEM) facility at the University of British Columbia (https://cryoem.med.ubc.ca). We thank Claire Atkinson, Amy Wo, Barathy Deivanayaga, Liam Worrall and Natalie Strynadka.

Funding and additional information

J.E.B. is supported by the Canadian Institute of Health Research (PJT-195808). A.L.S. was supported by a CIHR CGS-D scholarship. C.K.Y. is supported by CIHR (PJT-168907) and the Natural Sciences and Engineering Research Council of Canada (NGPIN-2024-04139). HRMEM is funded by the Canadian Foundation for Innovation and the British Columbia Knowledge Development Fund. J.A.C is supported by the Natural Sciences and Engineering Research Council of Canada (NGPIN-41822) and the Canadian Institute of Health Research (PJT-175120 AND PJT-175136).

Conflict of interest

J.E.B. reports research contracts from Calico Life Sciences and OmniAB therapeutics. The authors declare that they have no conflicts of interest with the contents of this article.

References

1. Balla, T. (2013) Phosphoinositides: Tiny Lipids With Giant Impact on Cell Regulation. *Physiological Reviews*. **93**, 1019–1137
2. Burke, J. E., Triscott, J., Emerling, B. M., and Hammond, G. R. V. (2023) Beyond PI3Ks: targeting phosphoinositide kinases in disease. *Nat Rev Drug Discov*. **22**, 357–386

858 3. Hammond, G. R. V., and Burke, J. E. (2020) Novel roles of phosphoinositides in
859 signaling, lipid transport, and disease. *Current Opinion in Cell Biology*. **63**, 57–67
860 4. Batrouni, A. G., and Baskin, J. M. (2021) The chemistry and biology of
861 phosphatidylinositol 4-phosphate at the plasma membrane. *Bioorganic and*
862 *Medicinal Chemistry*. **40**, 116190
863 5. de Rubio, R. G., Ransom, R. F., Malik, S., Yule, D. I., Anantharam, A., and Smrcka,
864 A. V. (2018) Phosphatidylinositol 4-phosphate is a major source of GPCR-stimulated
865 phosphoinositide production. *Sci Signal*. **11**, eaan1210
866 6. Chung, J., Torta, F., Masai, K., Lucast, L., Czapla, H., Tanner, L. B.,
867 Narayanaswamy, P., Wenk, M. R., Nakatsu, F., and De Camilli, P. (2015)
868 PI4P/phosphatidylserine countertransport at ORP5- and ORP8-mediated ER–
869 plasma membrane contacts. *Science*. **349**, 428–432
870 7. Lees, J. A., Zhang, Y., Oh, M. S., Schauder, C. M., Yu, X., Baskin, J. M., Dobbs, K.,
871 Notarangelo, L. D., De Camilli, P., Walz, T., and Reinisch, K. M. (2017) Architecture
872 of the human PI4KIIIα lipid kinase complex. *Proceedings of the National Academy of*
873 *Sciences of the United States of America*. **114**, 13720–13725
874 8. Dornan, G. L., Dalwadi, U., Hamelin, D. J., Hoffmann, R. M., Yip, C. K., and Burke,
875 J. E. (2018) Probing the Architecture, Dynamics, and Inhibition of the
876 PI4KIIIα/TTC7/FAM126 Complex. *Journal of Molecular Biology*. **430**, 3129–3142
877 9. Baskin, J. M., Wu, X., Christiano, R., Oh, M. S., Schauder, C. M., Gazzerro, E.,
878 Messa, M., Baldassari, S., Assereto, S., Biancheri, R., Zara, F., Minetti, C.,
879 Raimondi, A., Simons, M., Walther, T. C., Reinisch, K. M., and De Camilli, P. (2016)
880 The leukodystrophy protein FAM126A (hyccin) regulates PtdIns(4)P synthesis at the
881 plasma membrane. *Nature Cell Biology*. **18**, 132–138
882 10. Nakatsu, F., Baskin, J. M., Chung, J., Tanner, L. B., Shui, G., Lee, S. Y.,
883 Pirruccello, M., Hao, M., Ingolia, N. T., Wenk, M. R., and De Camilli, P. (2012)
884 Ptdins4P synthesis by PI4KIIIα at the plasma membrane and its impact on plasma
885 membrane identity. *Journal of Cell Biology*. **199**, 1003–1016
886 11. Suresh, S., Shaw, A. L., Pemberton, J. G., Scott, M. K., Harris, N. J., Parson, M.
887 A. H., Jenkins, M. L., Rohilla, P., Alvarez-Prats, A., Balla, T., Yip, C. K., and Burke,

888 J. E. (2024) Molecular basis for plasma membrane recruitment of PI4KA by EFR3.
889 *Science Advances*. **10**, eadp6660
890 12. Barlow-Busch, I., Shaw, A. L., and Burke, J. E. (2023) PI4KA and PIKfyve:
891 Essential phosphoinositide signaling enzymes involved in myriad human diseases.
892 *Current Opinion in Cell Biology*. **83**, 102207
893 13. Suresh, S., and Burke, J. E. (2023) Structural basis for the conserved roles of
894 PI4KA and its regulatory partners and their misregulation in disease. *Advances in*
895 *Biological Regulation*. **90**, 100996
896 14. Chen, R., Giliani, S., Lanzi, G., Mias, G. I., Lonardi, S., Dobbs, K., Manis, J., Im,
897 H., Gallagher, J. E., Phanstiel, D. H., Euskirchen, G., Lacroute, P., Bettinger, K.,
898 Moratto, D., Weinacht, K., Montin, D., Gallo, E., Mangili, G., Porta, F., Notarangelo,
899 L. D., Pedretti, S., Al-Herz, W., Alfahdli, W., Comeau, A. M., Traister, R. S., Pai, S.-
900 Y., Carella, G., Facchetti, F., Nadeau, K. C., Snyder, M., and Notarangelo, L. D.
901 (2013) Whole Exome Sequencing Identifies TTC7A Mutations for Combined
902 Immunodeficiency with Intestinal Atresias. *J Allergy Clin Immunol*. **132**, 656-664.e17
903 15. Agarwal, N. S., Northrop, L., Anyane-Yeboa, K., Aggarwal, V. S., Nagy, P. L.,
904 and Demirdag, Y. Y. (2014) Tetratricopeptide Repeat Domain 7A (TTC7A) Mutation
905 in a Newborn with Multiple Intestinal Atresia and Combined Immunodeficiency. *J*
906 *Clin Immunol*. **34**, 607–610
907 16. Yang, W., Lee, P. p. w., Thong, M.-K., Ramanujam, T. m., Shanmugam, A., Koh,
908 M.-T., Chan, K.-W., Ying, D., Wang, Y., Shen, J. j., Yang, J., and Lau, Y. l. (2015)
909 Compound heterozygous mutations in TTC7A cause familial multiple intestinal
910 atresias and severe combined immunodeficiency. *Clinical Genetics*. **88**, 542–549
911 17. Jardine, S., Dhingani, N., and Muise, A. M. (2019) TTC7A: Steward of Intestinal
912 Health. *Cellular and Molecular Gastroenterology and Hepatology*. **7**, 555–570
913 18. Zara, F., Biancheri, R., Bruno, C., Bordo, L., Assereto, S., Gazzerro, E., Sotgia,
914 F., Wang, X. B., Gianotti, S., Stringara, S., Pedemonte, M., Uziel, G., Rossi, A.,
915 Schenone, A., Tortori-Donati, P., van der Knaap, M. S., Lisanti, M. P., and Minetti,
916 C. (2006) Deficiency of hyccin, a newly identified membrane protein, causes
917 hypomyelination and congenital cataract. *Nat Genet*. **38**, 1111–1113

918 19. Biancheri, R., Zara, F., Rossi, A., Mathot, M., Nassogne, M. C., Yalcinkaya, C.,
919 Erturk, O., Tuysuz, B., Di Rocco, M., Gazzerro, E., Bugiani, M., van Spaendonk, R.,
920 Sistermans, E. A., Minetti, C., van der Knaap, M. S., and Wolf, N. I. (2011)
921 Hypomyelination and Congenital Cataract: Broadening the Clinical Phenotype.
922 *Archives of Neurology*. **68**, 1191–1194
923 20. Gazzerro, E., Baldassari, S., Giacomini, C., Musante, V., Fruscione, F., La
924 Padula, V., Biancheri, R., Scarfì, S., Prada, V., Sotgia, F., Duncan, I. D., Zara, F.,
925 Werner, H. B., Lisanti, M. P., Nobbio, L., Corradi, A., and Minetti, C. (2012) Hyccin,
926 the Molecule Mutated in the Leukodystrophy Hypomyelination and Congenital
927 Cataract (HCC), Is a Neuronal Protein. *PLoS ONE*. **7**, e32180
928 21. Berger, K. L., Cooper, J. D., Heaton, N. S., Yoon, R., Oakland, T. E., Jordan, T.
929 X., Mateu, G., Grakoui, A., and Randall, G. (2009) Roles for endocytic trafficking
930 and phosphatidylinositol 4-kinase III alpha in hepatitis C virus replication. *Proc. Natl.*
931 *Acad. Sci. U.S.A.* **106**, 7577–7582
932 22. Berger, K. L., Kelly, S. M., Jordan, T. X., Tartell, M. A., and Randall, G. (2011)
933 Hepatitis C virus stimulates the phosphatidylinositol 4-kinase III alpha-dependent
934 phosphatidylinositol 4-phosphate production that is essential for its replication. *J.*
935 *Virol.* **85**, 8870–8883
936 23. Adhikari, H., Kattan, W. E., Kumar, S., Zhou, P., Hancock, J. F., and Counter, C.
937 M. (2021) Oncogenic KRAS is dependent upon an EFR3A-PI4KA signaling axis for
938 potent tumorigenic activity. *Nat Commun*. **12**, 5248
939 24. Kattan, W. E., Liu, J., Montufar-Solis, D., Liang, H., Brahmendra Barathi, B., van
940 der Hoeven, R., Zhou, Y., and Hancock, J. F. (2021) Components of the
941 phosphatidylserine endoplasmic reticulum to plasma membrane transport
942 mechanism as targets for KRAS inhibition in pancreatic cancer. *Proc Natl Acad Sci*
943 *U S A*. **118**, e2114126118
944 25. Waring, M. J., Andrews, D. M., Faulder, P. F., Flemington, V., McKelvie, J. C.,
945 Maman, S., Preston, M., Raubo, P., Robb, G. R., Roberts, K., Rowlinson, R., Smith,
946 J. M., Swarbrick, M. E., Treinies, I., Winter, J. J. G., and Wood, R. J. (2014) Potent,
947 selective small molecule inhibitors of type III phosphatidylinositol-4-kinase α- but not

948 β-inhibit the phosphatidylinositol signaling cascade and cancer cell proliferation.
949 *Chem. Commun. (Camb.)*. **50**, 5388–5390
950 26. Bojjireddy, N., Botyanszki, J., Hammond, G., Creech, D., Peterson, R., Kemp, D.
951 C., Snead, M., Brown, R., Morrison, A., Wilson, S., Harrison, S., Moore, C., and
952 Balla, T. (2014) Pharmacological and genetic targeting of the PI4KA enzyme reveals
953 its important role in maintaining plasma membrane phosphatidylinositol 4-phosphate
954 and phosphatidylinositol 4,5-bisphosphate levels. *J Biol Chem*. **289**, 6120–6132
955 27. Hamers-Casterman, C., Atarhouch, T., Muyldermans, S., Robinson, G.,
956 Hammers, C., Songa, E. B., Bendahman, N., and Hammers, R. (1993) Naturally
957 occurring antibodies devoid of light chains. *Nature*. **363**, 446–448
958 28. Jin, B.-K., Odongo, S., Radwanska, M., and Magez, S. (2023) NANOBODIES®:
959 A Review of Diagnostic and Therapeutic Applications. *Int J Mol Sci*. **24**, 5994
960 29. Wu, X., Chi, R. J., Baskin, J. M., Lucast, L., Burd, C. G., DeCamilli, P., and
961 Reinisch, K. M. (2014) Structural Insights into Assembly and Regulation of the
962 Plasma Membrane Phosphatidylinositol 4-Kinase Complex. *Developmental Cell*. **28**,
963 19–29
964 30. Hornbeck, P. V., Zhang, B., Murray, B., Kornhauser, J. M., Latham, V., and
965 Skrzypek, E. (2015) PhosphoSitePlus, 2014: mutations, PTMs and recalibrations.
966 *Nucleic Acids Res.* **43**, D512-20
967 31. Yaron-Barir, T. M., Joughin, B. A., Huntsman, E. M., Kerelsky, A., Cizin, D. M.,
968 Cohen, B. M., Regev, A., Song, J., Vasan, N., Lin, T.-Y., Orozco, J. M., Schoenherr,
969 C., Sagum, C., Bedford, M. T., Wynn, R. M., Tso, S.-C., Chuang, D. T., Li, L., Li, S.
970 S.-C., Creixell, P., Krismer, K., Takegami, M., Lee, H., Zhang, B., Lu, J., Cossentino,
971 I., Landry, S. D., Uduman, M., Blenis, J., Elemento, O., Frame, M. C., Hornbeck, P.
972 V., Cantley, L. C., Turk, B. E., Yaffe, M. B., and Johnson, J. L. (2024) The intrinsic
973 substrate specificity of the human tyrosine kinome. *Nature*. **629**, 1174–1181
974 32. Kwon, J., Kim, D. H., Park, J. M., Park, Y. H., Hwang, Y. H., Wu, H.-G., Shin, K.
975 H., and Kim, I. A. (2016) Targeting Phosphatidylinositol 4-Kinase IIIα for
976 Radiosensitization: A Potential Model of Drug Repositioning Using an Anti-Hepatitis
977 C Viral Agent. *Int J Radiat Oncol Biol Phys*. **96**, 867–876

978 33. McMahon, C., Baier, A. S., Pascolutti, R., Wegrecki, M., Zheng, S., Ong, J. X.,
979 Erlandson, S. C., Hilger, D., Rasmussen, S. G. F., Ring, A. M., Manglik, A., and
980 Kruse, A. C. (2018) Yeast surface display platform for rapid discovery of
981 conformationally selective nanobodies. *Nat Struct Mol Biol*. **25**, 289–296
982 34. Shaw, A. L., Suresh, S., Parson, M. A. H., Harris, N. J., Jenkins, M. L., Yip, C. K.,
983 and Burke, J. E. (2024) Structure of calcineurin bound to PI4KA reveals dual
984 interface in both PI4KA and FAM126A. *Structure*. **32**, 1973-1983.e6
985 35. Abramson, J., Adler, J., Dunger, J., Evans, R., Green, T., Pritzel, A.,
986 Ronneberger, O., Willmore, L., Ballard, A. J., Bambrick, J., Bodenstein, S. W.,
987 Evans, D. A., Hung, C.-C., O'Neill, M., Reiman, D., Tunyasuvunakool, K., Wu, Z.,
988 Žemgulytė, A., Arvaniti, E., Beattie, C., Bertolli, O., Bridgland, A., Cherepanov, A.,
989 Congreve, M., Cowen-Rivers, A. I., Cowie, A., Figurnov, M., Fuchs, F. B., Gladman,
990 H., Jain, R., Khan, Y. A., Low, C. M. R., Perlin, K., Potapenko, A., Savy, P., Singh,
991 S., Stecula, A., Thillaisundaram, A., Tong, C., Yakneen, S., Zhong, E. D., Zielinski,
992 M., Žídek, A., Bapst, V., Kohli, P., Jaderberg, M., Hassabis, D., and Jumper, J. M.
993 (2024) Accurate structure prediction of biomolecular interactions with AlphaFold 3.
994 *Nature*. 10.1038/s41586-024-07487-w
995 36. James, E. I., Murphree, T. A., Vorauer, C., Engen, J. R., and Guttman, M. (2022)
996 Advances in Hydrogen/Deuterium Exchange Mass Spectrometry and the Pursuit of
997 Challenging Biological Systems. *Chem Rev*. **122**, 7562–7623
998 37. Masson, G. R., Jenkins, M. L., and Burke, J. E. (2017) An overview of hydrogen
999 deuterium exchange mass spectrometry (HDX-MS) in drug discovery. *Expert Opin*
1000 *Drug Discov*. **12**, 981–994
1001 38. Skinner, J. J., Lim, W. K., Bédard, S., Black, B. E., and Englander, S. W. (2012)
1002 Protein hydrogen exchange: testing current models. *Protein Sci.* **21**, 987–995
1003 39. Bojjireddy, N., Guzman-Hernandez, M. L., Reinhard, N. R., Jovic, M., and Balla,
1004 T. (2015) EFR3s are palmitoylated plasma membrane proteins that control
1005 responsiveness to G-protein-coupled receptors. *J Cell Sci*. **128**, 118–128
1006 40. Koester, A. M., Geiser, A., Laidlaw, K. M. E., Morris, S., Cutiongco, M. F. A.,
1007 Stirrat, L., Gadegaard, N., Boles, E., Black, H. L., Bryant, N. J., and Gould, G. W.

1008 (2022) EFR3 and phosphatidylinositol 4-kinase IIIα regulate insulin-stimulated
1009 glucose transport and GLUT4 dispersal in 3T3-L1 adipocytes. *Bioscience Reports*.
1010 **42**, BSR20221181
1011 41. Chung, J., Nakatsu, F., Baskin, J. M., and De Camilli, P. (2015) Plasticity of
1012 PI4KIIIα interactions at the plasma membrane. *EMBO reports*. **16**, 312–320
1013 42. Batrouni, A. G., Bag, N., Phan, H. T., Baird, B. A., and Baskin, J. M. (2022) A
1014 palmitoylation code controls PI4KIIIα complex formation and PI(4,5)P2 homeostasis
1015 at the plasma membrane. *J Cell Sci*. **135**, jcs259365
1016 43. Beghein, E., and Gettemans, J. (2017) Nanobody Technology: A Versatile Toolkit
1017 for Microscopic Imaging, Protein-Protein Interaction Analysis, and Protein Function
1018 Exploration. *Front Immunol*. **8**, 771
1019 44. Koenig, P.-A., Das, H., Liu, H., Kümmerer, B. M., Gohr, F. N., Jenster, L.-M.,
1020 Schiffelers, L. D. J., Tesfamariam, Y. M., Uchima, M., Wuerth, J. D., Gatterdam, K.,
1021 Ruetalo, N., Christensen, M. H., Fandrey, C. I., Normann, S., Tödtmann, J. M. P.,
1022 Pritzl, S., Hanke, L., Boos, J., Yuan, M., Zhu, X., Schmid-Burgk, J. L., Kato, H.,
1023 Schindler, M., Wilson, I. A., Geyer, M., Ludwig, K. U., Hällberg, B. M., Wu, N. C.,
1024 and Schmidt, F. I. (2021) Structure-guided multivalent nanobodies block SARS-
1025 CoV-2 infection and suppress mutational escape. *Science*. **371**, eabe6230
1026 45. Fischer, B., Uchański, T., Sheryazdanova, A., Gonzalez, S., Volkov, A. N.,
1027 Brosens, E., Zögg, T., Kalichuk, V., Ballet, S., Versées, W., Sablina, A. A., Pardon,
1028 E., Wohlkönig, A., and Steyaert, J. (2024) Allosteric nanobodies to study the
1029 interactions between SOS1 and RAS. *Nat Commun*. **15**, 6214
1030 46. Weissmann, F., Petzold, G., VanderLinden, R., Huis In't Veld, P. J., Brown, N.
1031 G., Lampert, F., Westermann, S., Stark, H., Schulman, B. A., and Peters, J. M.
1032 (2016) BiGBac enables rapid gene assembly for the expression of large multisubunit
1033 protein complexes. *Proceedings of the National Academy of Sciences of the United*
1034 *States of America*. **113**, E2564–E2569
1035 47. Gibson, D. G., Young, L., Chuang, R. Y., Venter, J. C., Hutchison, C. A., and
1036 Smith, H. O. (2009) Enzymatic assembly of DNA molecules up to several hundred
1037 kilobases. *Nature Methods*. **6**, 343–345

1038 48. McMahon, C., Baier, A. S., Pascolutti, R., Wegrecki, M., Zheng, S., Ong, J. X.,
1039 Erlandson, S. C., Hilger, D., Rasmussen, S. G. F., Ring, A. M., Manglik, A., and
1040 Kruse, A. C. (2018) Yeast surface display platform for rapid discovery of
1041 conformationally selective nanobodies. *Nat Struct Mol Biol*. **25**, 289–296
1042 49. Stariha, J. T. B., Hoffmann, R. M., Hamelin, D. J., and Burke, J. E. (2021)
1043 Probing Protein-Membrane Interactions and Dynamics Using Hydrogen-Deuterium
1044 Exchange Mass Spectrometry (HDX-MS). *Methods Mol Biol*. **2263**, 465–485
1045 50. Dobbs, J. M., Jenkins, M. L., and Burke, J. E. (2020) Escherichia coli and Sf9
1046 Contaminant Databases to Increase Efficiency of Tandem Mass Spectrometry
1047 Peptide Identification in Structural Mass Spectrometry Experiments. *J Am Soc Mass*
1048 *Spectrom*. **31**, 2202–2209
1049 51. Kong, A. T., Leprevost, F. V., Avtonomov, D. M., Mellacheruvu, D., and
1050 Nesvizhskii, A. I. (2017) MSFragger: ultrafast and comprehensive peptide
1051 identification in mass spectrometry-based proteomics. *Nat Methods*. **14**, 513–520
1052 52. Masson, G. R., Burke, J. E., Ahn, N. G., Anand, G. S., Borchers, C., Brier, S.,
1053 Bou-Assaf, G. M., Engen, J. R., Englander, S. W., Faber, J., Garlish, R., Griffin, P.
1054 R., Gross, M. L., Guttman, M., Hamuro, Y., Heck, A. J. R., Houde, D., Iacob, R. E.,
1055 Jørgensen, T. J. D., Kaltashov, I. A., Klinman, J. P., Konermann, L., Man, P.,
1056 Mayne, L., Pascal, B. D., Reichmann, D., Skehel, M., Snijder, J., Strutzenberg, T.
1057 S., Underbakke, E. S., Wagner, C., Wales, T. E., Walters, B. T., Weis, D. D., Wilson,
1058 D. J., Wintrode, P. L., Zhang, Z., Zheng, J., Schriemer, D. C., and Rand, K. D.
1059 (2019) Recommendations for performing, interpreting and reporting hydrogen
1060 deuterium exchange mass spectrometry (HDX-MS) experiments. *Nat. Methods*. **16**,
1061 595–602
1062 53. Perez-Riverol, Y., Bai, J., Bandla, C., García-Seisdedos, D., Hewapathirana, S.,
1063 Kamatchinathan, S., Kundu, D. J., Prakash, A., Frericks-Zipper, A., Eisenacher, M.,
1064 Walzer, M., Wang, S., Brazma, A., and Vizcaíno, J. A. (2022) The PRIDE database
1065 resources in 2022: a hub for mass spectrometry-based proteomics evidences.
1066 *Nucleic Acids Res*. **50**, D543–D552

1067 54. Bates, T. A., Gurmessa, S. K., Weinstein, J. B., Trank-Greene, M., Wrynla, X. H.,
1068 Anastas, A., Anley, T. W., Hinchliff, A., Shinde, U., Burke, J. E., and Tafesse, F. G.
1069 (2025) Biolayer interferometry for measuring the kinetics of protein-protein
1070 interactions and nanobody binding. *Nat Protoc*. **20**, 861–883
1071